Department of Precision and Microsystems Engineering

Thermal process modelling of lattice structures during selective laser melting process

Yaqian Zhong

Report no : EM-2021.066
Coach : Can Ayas
Professor : Prof.dr.ir. A. (Fred) van Keulen
Specialisation : SOM
Type of report : Master Thesis
Date : 20/08/2021

Yaqian Zhong 4752168

Thermal process modelling of lattice structures

during selective laser melting process

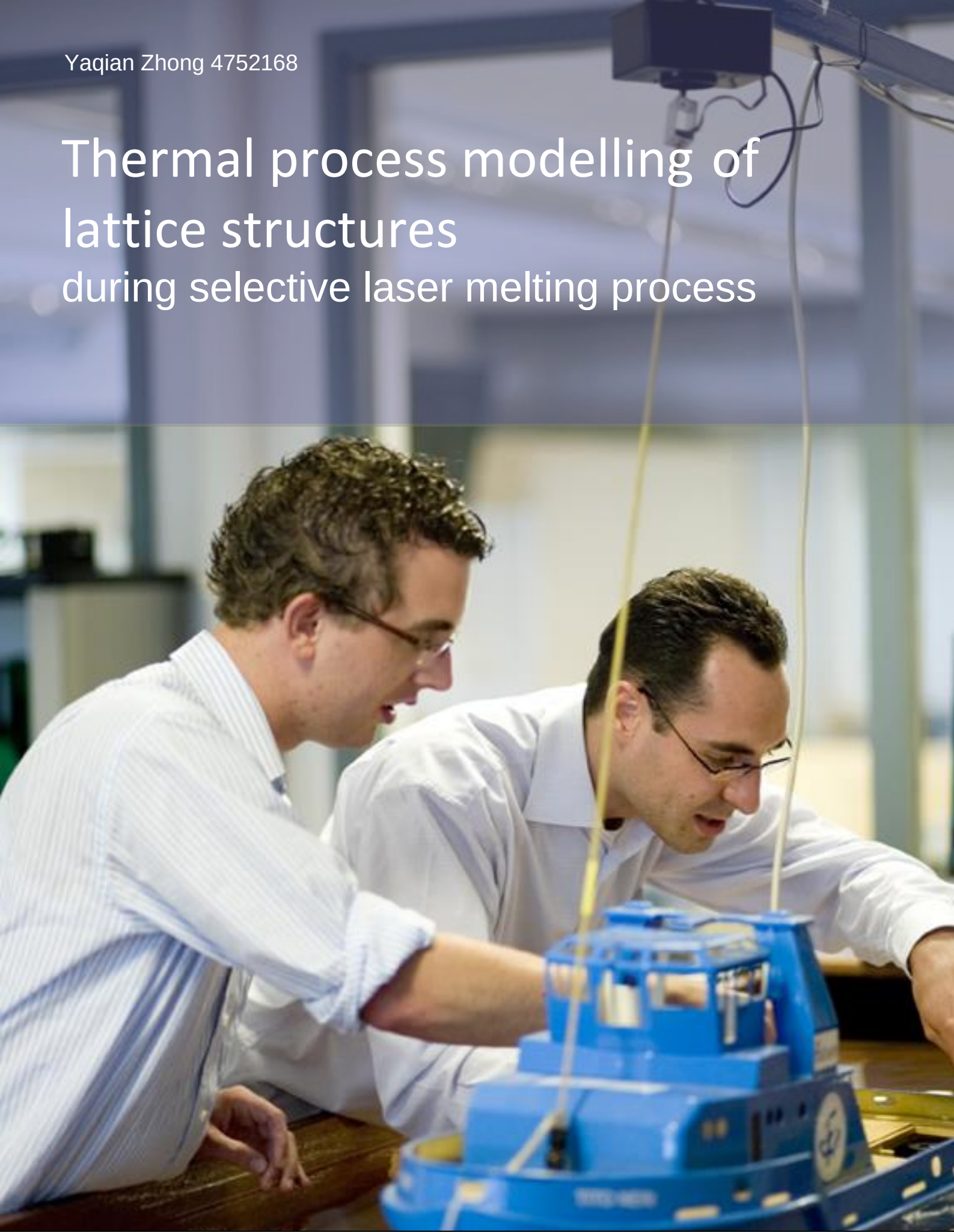

TU Delft Delft University of Technology

Structural Optimization and Mechanics

ABSTRACT

As a type of powder-bed-based Additive Manufacturing (AM), Selective Laser Melting (SLM) is widely used for building metallic lattice structures. However, during SLM process, geometrical imperfections and defects, such as strut over-sizing or under-sizing, typically exist in components due to overheating, which strongly influence their mechanical response. Therefore, it is common that the as-built lattice has discrepancies from the designed lattice structure in mechanical properties. The main aim of this study is to simulate the transient temperature field of lattices during SLM process to predict the possible manufacturing issues for the improvement of product quality. Based on a technique, the moving grid method, growing struts of a lattice whilst it being built by SLM can be regarded as moving domain problems, and thermal process of a building lattice can be simulated numerically. The primary contribution of this study is to evaluate the effect of process parameters, including laser power, energy density and material deposition rate, on thermal evolution of a lattice during SLM. Another contribution is related to the comparison of transient temperature field between different lattice architectures. Analyzing the influences of various factors is important to recognize the thermal evolution of a building lattice. The results reported in this study offer a reference for quality improvement of produced parts, to realize that both geometry and mechanical properties of the as-built lattices as close as possible to their as-designed counterparts.

SUMMARY

It is well-known that SLM technique has the potential for fabrication of intricate geometries, especially for lattice materials characterized by a set of struts that connect the nodes of the lattice. However, only limited investigation into SLM of lattice structures for their transient thermal performance, such as heat transfer, have been undertaken to date. In this work, based on a novel moving grid method, a thermal modelling approach for the thermal field of a SLM-processed lattice structure is developed.

In fact, accurately model the development of temperature for a lattice structure whilst it being built by SLM is extremely challenging. The real SLM is a complex process and strongly depend on varying process parameters and scanning strategies. There are several of process-related assumptions are made in this study for problem simplification. First, Regardless of the scanning strategy due to our model in a 2D plane. The heat load from the laser source is assumed to be applied simultaneously on a whole component surface orthogonal to the building direction (i.e., the plane on the cross section of the component). Second, thermal radiation and thermal conduction between the metallic powder and consolidated part are not involved when considering the heat transfer behavior of a SLM-processed lattice. Besides, the thermodynamic properties of the chosen material, Ti-6Al-4V, are all assumed as temperature-independent. In addition, it is further assumed that the simulated lattice structure consists of idealized struts with a perfect square cross section.

Based on the assumption stated above, We first proposed a 1D model for a single lattice member to explain the moving grid method. Different from the traditional Finite Element approach, the basic idea of the moving gird method is using a constant number of nodes with an increased spatial nodal interval to describe the length growth of the lattice struts whilst they being built by SLM. Following the same mechanism, such 1D strut model is expanded to 2D domain for a lattice geometry. After that, by defining the governing equations and the corresponding thermal boundary conditions for a specific lattice structure during both the heating stage and the cooling stage of the SLM process, the temperature evolution for every lattice strut in each time step can be simulated.

Particularly, using the developed thermal model one can quantify the effects of process parameters in combination with the lattice architecture, on the development of the temperature evolution. For this purpose, simulations are carried out with different sets of process parameters for different lattice structures. To be more specific, three basic types of lattice structures are considered in this work: the triangular lattices, the square lattices, and the hexagonal lattices. The contributions of a lattice topology on the thermal results are investigated in terms of four aspects: the elementary cell configuration, the unit cell size, the lattice orientation, and the total amount of connectivity of a lattice structure (Nc). Furthermore, four parameters among various process parameters are chosen for the evaluation, which involving the energy density VED, the material deposition rate $\dot{V}$, the cooling duration λ, and the Biot number Bi. Eventually, a convergence study is performed to examine the reliability of the obtained thermal results. Meanwhile, it also enables a comprehensive analysis for balancing the result accuracy and the computational efficiency.

Contents

List of Figures

LIST OF TABLES

ACKNOWLEDGEMENTS

Many people have offered me valuable help in my thesis writing, including my tutor, my friends, and my parents.

Firstly, I would like to give my sincere gratitude to my supervisor Dr. Can Ayas, who with extraordinary patience and guidance on my thesis. He gave me great help by providing me with necessary material and significant advice when I was encountered the difficulty.

Then, I deeply appreciate the contribution of my friends, who have continuously been encouraging me without a word of complaint.

I would like to express my appreciation to my parents for their support. They provide finical support for me to study and live in a foreign country.

Eventually, special thanks should go to my dearest Weizhao. We met at a toughest time for me, his companionship has sustained me through depression. I feel extremely grateful to his consistent support and care for me.

1

INTRODUCTION

1

1.1. BACKGROUND

ADDITIVE manufacturing (AM) is an emerging field in manufacturing technologies to build up solid parts through material addition in a layer by layer manner [1]. It enables fabrication of geometrically complex metal products with a minimum need for post-processing and has the potential to approach near-zero material waste [2]. In contrast to traditional manufacturing techniques such as machining, milling and casting, AM offers almost unlimited design freedom and provides an economical way for designers and engineers to create unique parts directly from computer-aided design (CAD) data [3]. Recently, AM has gathered much interest in industry and academia due to the increased industrial demand for highly customized parts [4]. Forecast for AM market is to dramatically grow from USD 8.35 billion in 2019 to USD 23,75 billion in 2027 [5].

Powder bed fusion (PBF) is one of the various AM methods that apply thermal energy to melt and fuse metallic powder instead of merely sintering it [6]. Common PBF methods including selective laser melting (SLM) and selective electron beam melting (SEBM). Figure 1.1 shows the specific printing process of these two PBF techniques that consists of the following steps [7]:

- The current layer of a metallic powder bed is heated up to the preheating temperature (SLM usually without the preheating step).
- An energy source (laser/electron beam) melts the target region of the metal component cross section.
- The platform is lowered by a layer thickness to accommodate the new layer.
- A new layer of metallic powder is spread over the platform.

Steps 1-4 are repeated until a complete part is formed.

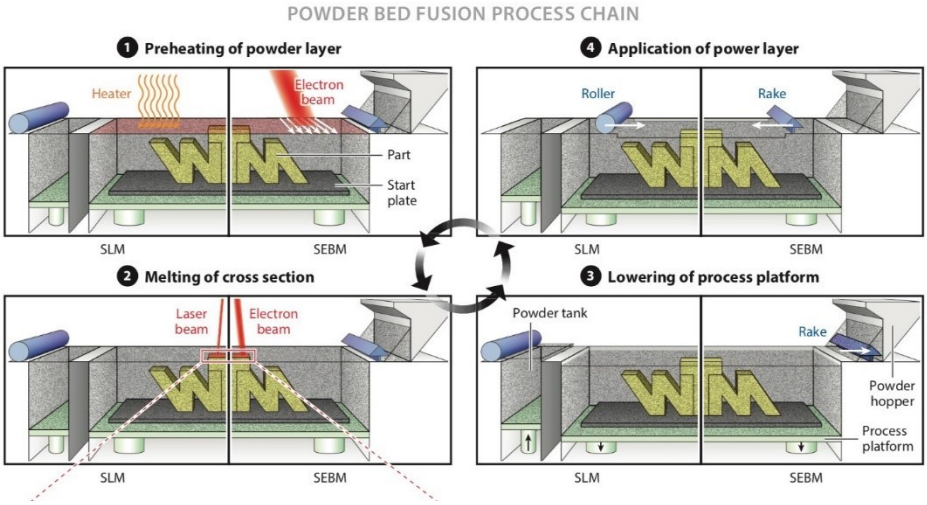

Figure 1.1: Steps of printing process for SLM and SEBM processes, reproduced from [8]. For each subpanels, SLM is shown on the left and SEBM on the right. Specifically, the process details are described as following: 1. each layer of a metallic powder bed is heated up to the preheating temperature; 2. the target region of the component cross section is melted; 3. the process platform is lowered by a unit layer thickness; 4. a new powder layer is spread and then the process restarts.

This study focuses on SLM, which utilizes laser as the energy source for selectively melting metallic powder to form individual layers of a three-dimensional part [9]. SLM technology enables the production of highly complex components, such as lattice materials that are challenging to be realized

by alternative manufacturing approaches [10]. Lattice structures are cellular materials comprising repeating unit cells and tessellating the space [11]. These unit cells are composed of slender beams or struts that are rigidly connected to each other. The mechanical properties of a lattice are tailored by modifying its architecture, for instance unit cell topology (connectivity) or geometry (cell size, strut orientations and dimensions). Consequently, lattice structures can be designed to provide unique properties that are unachievable by their bulk counterparts [12]. Moreover, lattice structures have high strength-to-weight ratio that can provide advanced performance for high value engineering products [13]. Based on these superior characteristics, lattices have widely used for industrial applications such as automobile, medical and aerospace industries in recent years.

1.2. PROBLEM STATEMENT

IN general, the geometries of additively fabricated lattices by SLM process are departing from their as-designed counterparts. In other words, the quality of the product cannot fully meet the target properties of the designed lattices. These discrepancies on dimensions are called geometric defects, for instance strut waviness, strut over-sizing or under-sizing. The mechanical response of the additively manufactured lattice can be significantly altered by these geometric imperfections. Unexpected mechanical properties might be induced due to such manufacturing issues, which might lead to unacceptable product performance. Thermal evolution of a component during SLM process has strong effects on its geometric imperfections. For example, overheating during the SLM process will lead to a thicker strut and non-uniform cross section along its length axis. In addition, thermal gradients generate distortion and residual stresses, which also leads to geometric imperfections [14]. Hence, thermal analysis of a lattice during SLM can be vitally insightful to ensure the as-built lattices achieving the mechanical performance of as-designed counterparts.

There are many possible factors having impact on the thermal response of a lattice during SLM. For example, process parameters, lattice architectures, and the choice of material. This dissertation mainly addresses the first two aspects. The geometric imperfections strongly depend on process parameters of SLM, which are chosen before the manufacturing process, such as laser power and scanning speed [15]. Besides, the architecture of the lattice also has an eminent role in the outcome of its thermal history during the SLM process. Note that a special term so-called elementary cell is discussed in this work, which is defined as the minimum cell of a lattice structure. Distinct from a unit cell, an elementary cell no need to be the repeating unit in a lattice structure. Three types of 2D lattice structures classifying according to the shape of their elementary cell are selected for investigation: triangular lattices, square lattices, and hexagonal lattices. In addition, based on these three kinds of SLM lattice structures, the lattice architecture can be altered by rotating its structure whilst keeping the shape of its elementary cell. For example, a square elementary cell becomes a rhombic elementary cell when it is rotated 45 degrees in the located 2D plane, and a rhombic lattice structure instead of the original square lattice is generated.

As mentioned above, geometric imperfections of lattices during SLM may directly depend on the thermal characteristics, such as the transient temperature field and thermal gradient. Therefore, thermal analysis enables a better understanding of the possible defects of an additively manufactured lattice material. Besides, investigating the effects of process parameters for various lattice structures on the thermal history provides a reference for quality prediction and improvement. For example, the manufacturing issues can be effectively minimized by finding an optimal set of process parameters. To examine the effects of process parameters and lattice topolpgy on product quality, the typical experimental approach is time consuming and expensive. In contrast, computational modelling is an economic and accessible approach for predicting the evolution of transient temperature of lattices during SLM [16]. In summary, the aims of this project are developing

1

a numerical model to simulate the transient temperature field of growing lattice material and evaluating the influence of lattice architectures, process parameters on the thermal evolution.

1.3. MOTIVATION

In fact, computational modelling brings a new problem. The physical characteristics of a component can be precisely captured by using very fine spatial discretizations. Moreover, for the transient temperature problems of interest, to accurately model the large amounts of repeated heating and cooling cycles during SLM, a very fine temporal resolution is required. Such high spatial and temporal resolution can lead to prohibitive computing time for a numerical modelling approach. Hence, developing an efficient numerical model for a SLM-processed lattice structure is crucial and numerous studies have been undertaken to develop more efficient approaches for modelling the AM processes.

One common way is developing a semi-analytical model instead of a fully numerical model. In general, the superposition principle is used to compute the temperature evolution in finite bodies. Specifically, a superposition of a temperature field due to the heat source (well-known in analytical form) and a numerically solved complimentary field to impose the boundary conditions is considered [17,18]. Herein both a point heat source [17] or a line heat source [18] can be chosen to precisely represent the laser scanning vector of SLM, and then a corresponding temperature field can be derived. In this regard, it is possible that a coarse spatial resolution is sufficient for an accurate numerical solution as the steep thermal gradiens can be accounted for analytically. Although the semi-analytical approach has superior performance on enhancing the computational efficiency, it is typically applied in a semi-infinite space. In contrast, a lattice structure has intricate geometry and not a semi-infinite body. Therefore, other possible approaches need to be investigated to develop a computationally efficient thermal model for lattices during SLM.

However, the complex geometry of lattice materials contributes to the difficulty in the efficient simulation. Although manufacturing of lattices by SLM has received significant attention in recent years, most of the studies concern about thermal modelling approaches for parts with relatively simpler geometry than lattice structures. To overcome this knowledge gap, this paper introduces a new approach to develop an efficient numerical model for lattice materials during SLM. This new technique, which is so-called moving grid method, is proposed by Guduru to solve moving boundary problems [19]. Consider now a 1D domain has an initial length l_0, which is discretized by n nodes and $n-1$ spatial intervals. In general, when such 1D domain is growing, an increased number of spatial intervals (i.e., the grid) is applied in the discretization scheme while the size of these intervals is constant with respect to time. In contrast, the essential idea of the moving grid method is keeping the number of grids $n-1$ to be constant while increase the size of each spatial interval in the time domain as expressed in Figure 1.2. After that, the solution on i^{th} node on the moving domain as given in Figure 1.2 can be calculated by the Finite Difference (FD) approximation. Compared with the general approach, this moving grid technique has excellent performance on enhancing computational efficiency. The main reason is the number of degrees of freedom for discretizing a moving domain is preserved by the fixed number of grids. Apparently, the required computing time for fewer degrees of freedom will be dramatically reduced.

Our thermal model is building on this moving grid method by regarding each strut during SLM as a 1D moving domain. Similarly, we consider each strut of a lattice has a growth velocity $\dot{l}$ on its length depending on the SLM process parameters, and a constant number of grid points are ap-

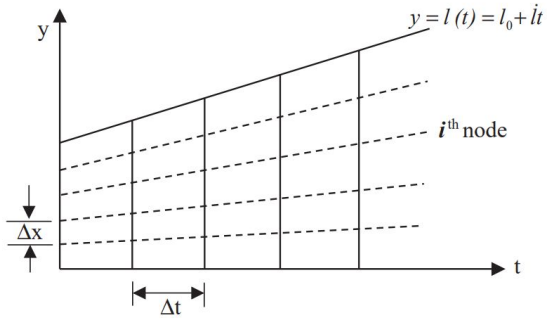

Figure 1.2: Scheme of the moving grid method, reproduced from [19]. A 1D boundary is growing from an initial length l_0 with with a length growth rate $\dot{l}$ for every time step Δt. Six nodes are used to discretize the boundary into five grids. The number of grid is constant with respect to time t while the spatial intervals Δx is increased in the time domain.

plied for the discretization. On the basis of that, solving the 1D heat equation by Finite Difference (FD) technique and the temperature evolution at every grid point for a single strut can be determined. For a 2D lattice that comprising many struts, the connectivity and heat transfer between struts need to be accounted for. Further details about expanding the 1D strut model to a 2D lattice model will be involved in Chapter 3. Based on this computationally efficient thermal model, the temperature history of a certain lattice structure during SLM can be simulated. Besides, the effects of lattice architecture and process parameters on the thermal evolution can be investigated.

In Chapter 2, modelling approaches in different scales for a lattice during SLM are discussed. Chapter 3 explains the methodology to apply the moving grid method and thermal process model for printing lattices with SLM. Chapter 4 presents the results obtained from the proposed numerical modelling approach. On the basis of these results, the influence of process parameters and architecture of lattice structures are evaluated in this section. Chapter 5 briefly concludes the investigations and recommendations for future work.

2

MODELLING APPROACHES FOR SLM

SLM process typically operates with a layer thickness ranging between 20–100 μm and the typical laser spot radius is tens of micrometers, while the parts built can be centimeters [20]. These two characteristics indicate that, building a part by SLM may require melting and fusing hundreds or thousands of layers of metallic powder, and such high resolution introduces an enormous printing time. Figure 2.1 clearly demonstrates the relationship between models in different length scales and the required characteristic modelling time. Modelling approaches in different scales use various level of assumptions and approximations, thus the observations on the basis of their simulation results are different. In this section, the details about the powder-scale models and continuum models for SLM will be discussed.

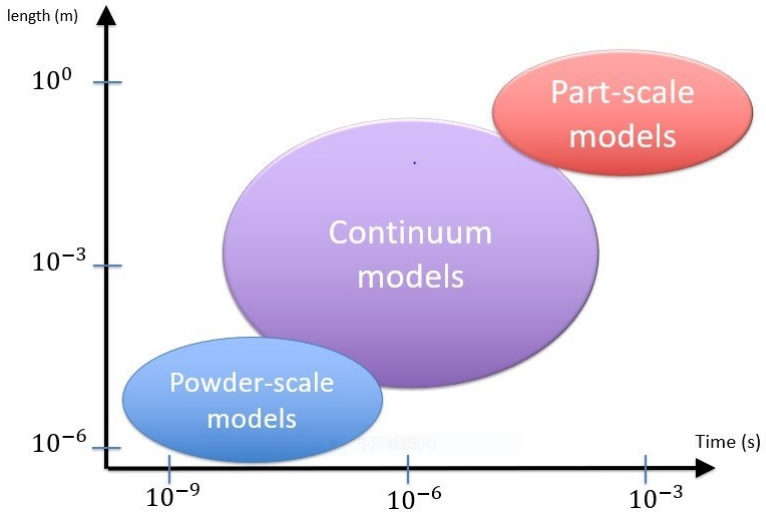

Figure 2.1: Schematic of modelling approaches for SLM in different scales. The relationship between the model scales and their corresponding ranges of length scale and modelling time scale are clearly defined.

2.1. COMPUTATIONAL EFFICIENCY OF A BUILDING LATTICE MODEL

THE aim of this study is predicting the transient temperature results by systematically modelling the lattice structures manufactured by SLM. In this regard, a part-scale model is demanded to simulate the thermal evolution of a lattice structure. Furthermore, enhancing the computational efficiency is a crucial challenge when developing the thermal model. As stated in the early stage, a completed SLM process needs a huge number of powder layers to finish a part. Typically, the layer thickness and spot radius both have extremely small values comparing to the part dimensions. Thus, a very fine spatial discretization is required to achieve the temperature transients with numerical approaches. Besides, large thermal gradients generally occur in the vicinity of the laser spot when it melting a certain layer of metallic powder, which has significant impact on the temperature evolution. To precisely determine the steep temperature gradients in a numerical way, the required number of temporal and spatial resolution can be enormous, which results in a large number of degrees of freedom (DOFs) and then prohibitive computational cost.

Consider now the model for lattice materials of interest. Lattices usually composed of a large number of struts, and Figure 2.2 shows some common types of lattice structures. To achieve a precise in-situ temperature measurement along each strut element, the spatial steps used for discretization should be sufficiently small comparing to the dimensions of a single strut. As the lattice model involves a lot of strut elements and in a much larger length scale, a very fine spatial discretization is used when modelling a lattice structure in part-scale, which implies higher number of DOFs. Taking the Finite Element (FE) method as an example, Figure 2.3 illustrates the effect of

the number of DOFs in the system on Central Processing Unit (CPU) time when a FE approach is employed to solve for lattice models. That is to say, the computational cost associated with high accuracy results is excessively high due to the extremely fine mesh. Meanwhile, significant number of temporal resolution is needed for ensuring the accuracy of the captured transient temperatures. Instead of the solid elements for the FE approach, grids are used in the finite difference discretization scheme to mesh the lattice struts and the statement implied in Figure 2.3 also true for the FD approach. Hence, modelling a growing lattice part will demand extensive computational resource and reducing computational cost while ensuing result accuracy can be challenging.

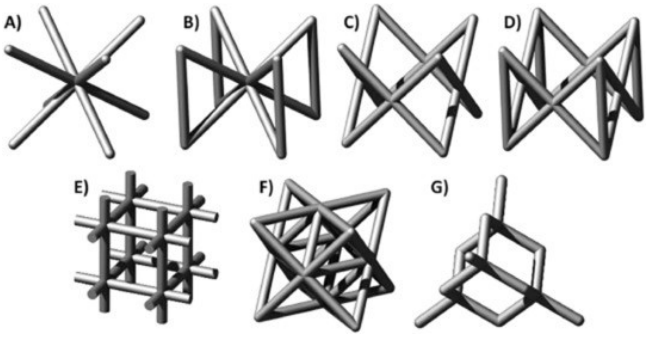

Figure 2.2: Strut-based lattice structures, reproduced from [21]: BCC (A), BCCZ (B), FCC (C), FCCZ (D), cubic (F), Octet-truss (G), and diamond (H).

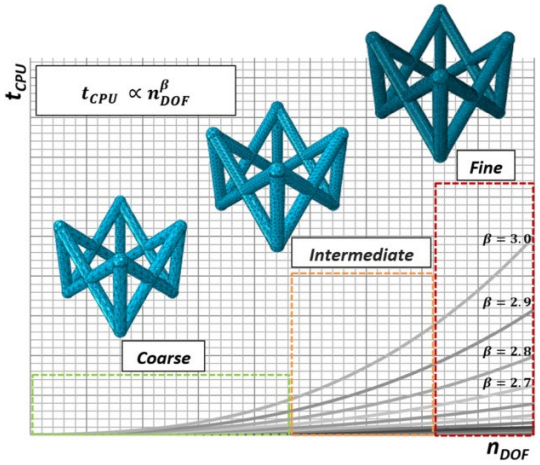

Figure 2.3: Schematic of relationship between CPU time, t_{CPU}, required to solve a finite element lattice model with corresponding DOF, n_{DOF}, reproduced from [22]. Representative images of lattice structure models with coarse, intermediate and fine meshes are shown, respectively. The exponent, β, is a constant typically between 2 and 3 for linear elastic FE models.

2.2. POWDER-SCALE APPROACHES

As introduced earlier, SLM is a type of powder-bed-based additive manufacturing technique, which fabricates component by the layer-wise fusion of metallic powder. Laying and melting the powder layer are the two fundamental procedures of SLM. During cyclic melting and solidification processes, various physical behaviors have crucial impact on the microstructure and mechanical properties of the component. For instance, recoil pressure, surface tension, and heat transfer involving conduction, convection and radiation, are the physical behaviors as schematically depicted in Figure 2.4 [23]. This section focuses on the powder-scale numerical approaches dealing with these physical phenomena, and providing insights into the surface morphology evolution and defects formation of the component. Typically, the numerical models in powder-scale

requiring the spatial resolutions on the order of micrometers. The so-called powder-scale refers to model the morphology of the metallic particles and concerns the interaction between the laser source and the powders [24]. It mainly includes two parts: the powder bed generation and the molten pool dynamics. For a modelling approach for SLM process in powder-scale, the interested domain often limited to particles within a single-track on a powder layer in microscale or mesoscale [8], and most of important hydrodynamic effects during processing can be studied in this domain, such as molten pool dynamic, surface tension, Marangoni effect, and vapor recoil.

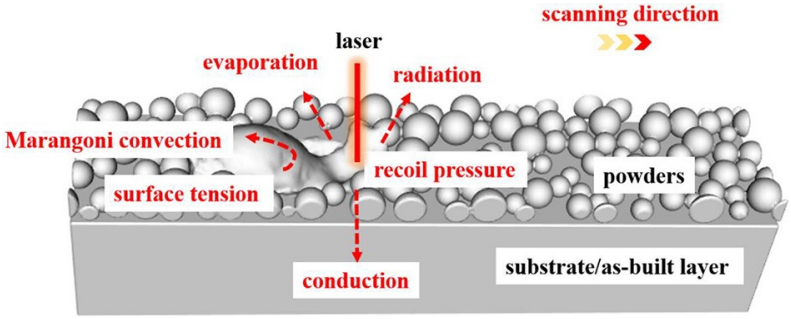

Figure 2.4: Schematic of underlying physical phenomena of during the SLM process in powder-scale, reproduced from [23]. Heat transfer will occur due to heat convection, heat conduction and radiation.

During SLM, new powder particles are distributed into the build tank to accommodate a new layer. In the powder-scale model, the individual particle is simplified as ideal spheres with different radii. The particle size and distribution are critical since they affect powder bed density and powder fluidity – which, in turn, affect component quality [25]. A typical approach to model the powder bed generation process is utilizing the discrete element method (DEM) software YADE [26,27,28], in which the powder particle size follows the distribution as shown in Figure 2.5.

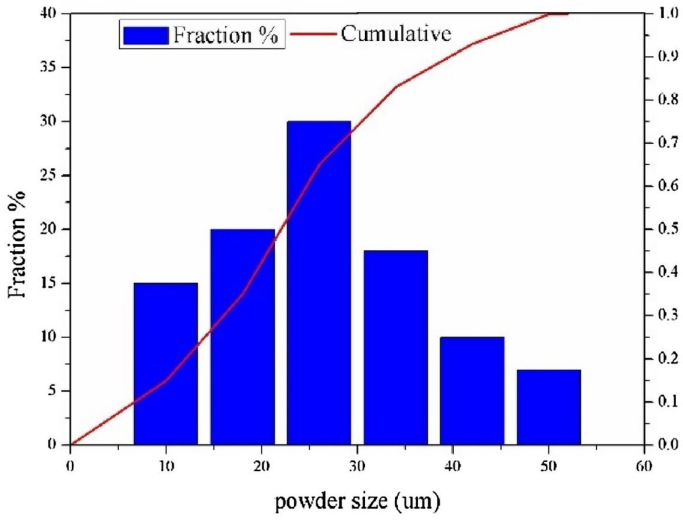

Figure 2.5: Description of the distribution of powder size of 316L particles during SLM, reproduced from [26].

In general, the laser heat source applied to the powder surface during SLM is modeled as a moving heat source with the Gaussian distribution in most of the studies [26,29,30]. This Gaussian moving heat source models that the heat source moves along the scanning path, and powder is melted ahead of the laser beam while solidified in the back. During SLM, most photons of the laser beam are reflected, and only a fraction of each reflection are absorbed to a depth of several nanometers [31]. Based on that, a numerical approach called ray tracing model is developed to use a finite

number of rays to divide the laser beam and then track their reflection routines as demonstrated in Figure 2.6 [29].

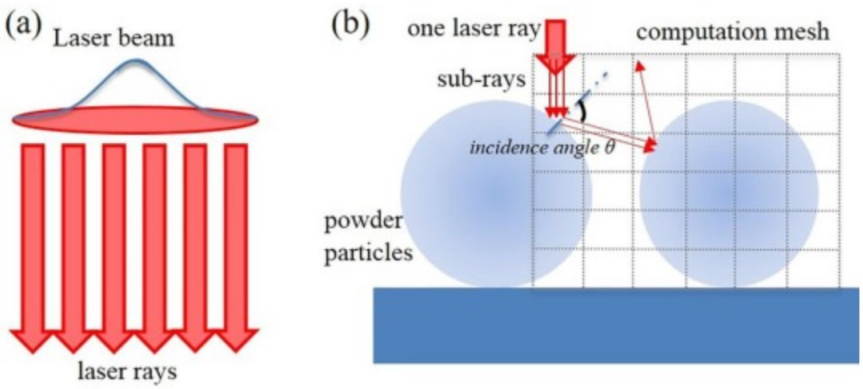

Figure 2.6: Ray tracing model, reproduced from [29]. (a) Laser beam is divided into rays. (b) The multi-reflection of each ray (containing sub-rays) is tracked, and the decrease of the number of sub-rays after each reflection corresponds to the part of the energy being absorbed.

During the melting process, a molten pool is formed. To identify the molten pool dynamic, it is crucial to account for the surface tension between melt and particles, coupling between gas phase and the metallic liquid, buoyancy, viscosity, heat dissipation, Marangoni effect, gasification recoil [32]. The heat loss during SLM can be contributed by evaporation conduction, convection and radiation. The differences in surface tension due to the large temperature gradient called Marangoni effect [33]. The Marangoni forces induce the melt to move from the temperature peak in the center to the edge of the molten pool [26,27]. Once the temperature of a molten pool is continuously increasing and higher than the evaporating point, the recoil pressures appears and additionally drive the fluid motion [28,29]. Both the Marangoni effect and the gasification recoil force strongly impact the shape and dynamic behavior of the molten pool. The conventional approach to simulate the molten pool dynamic is using the governing equations based on the Navier-Strokes equations [29,32]. The governing equations include the conservation equation of mass, momentum and energy, are solved using the finite difference (FD) method to predict the dynamic behavior of the SLM molten pool.

Massive researches developed microscopic or mesoscopic numerical models for SLM combined with the above theoretical model for the physical behaviors. This high-fidelity powder scale model can detailed describe the SLM formation process, and the formation of defects can be predicted, for instance, pores and balls [26,34,35]. However, the powder-scale models usually require very fine meshes to resolve the individual powder particle, and thus their computing cost are often huge. Therefore, the powder-scale models for SLM are usually limited to the single-track domain or single-layer domain and inapplicable for a reasonable part dimension.

2.3. CONTINUUM APPROACHES

To model the SLM process, the powder-scale models is aiming to understand the surface morphology on a powder layer and offer a full description of the component microstructure. As mentioned in the previous section, the computational cost is prohibitively high to simulate the powder-scale models for SLM. The powder-scale models usually have a characteristic length at the level of microscopic or mesoscopic, as exhibited in Figure 2.7. In contrast, the part-scale models at the level of macroscopic can effectively reduce the computational effort as it simulates the thermal response in considerably larger domain with sizes ranging from 10 mm to 1000 mm. On the

other hand, they have failed to directly provide a precise microstructure representation [36]. The continuum model for SLM has a scale between the powder-scale models and part-scale models at the level of mesoscopic or macroscopic. In general, continuum models enforce many simplifying assumptions. One of the assumptions is that the powder bed is treated as an effective continuum, and then the equivalent thermophysical parameters and equivalent flow behavior model are considered to describe the SLM process [37]. In addition, the hydrodynamics between particles considered in the powder-scale models and the effect of localized phase change are neglected [38,39]. Rather than a single-track domain in powder-scale models, the domain of interest for continuum approaches is increasing to multi-tracks and multi-layers. Compared with the powder-scale modelling approaches, the continuum models enable a compromise between the computational cost and the description of the microstructure by treating the powder bed as a continuum and no need to resolve the particles. They are beneficial to define a simpler interface between the material powder and the atmosphere to decrease the spatial and temporal resolution [8]. In the continuum models, the minimum mesh size is limited by the single layer thickness. Since it is possible that several layers are combined to one composite layer, the minimum element size can be increased and larger application domains up to the part-scale can be realizable.

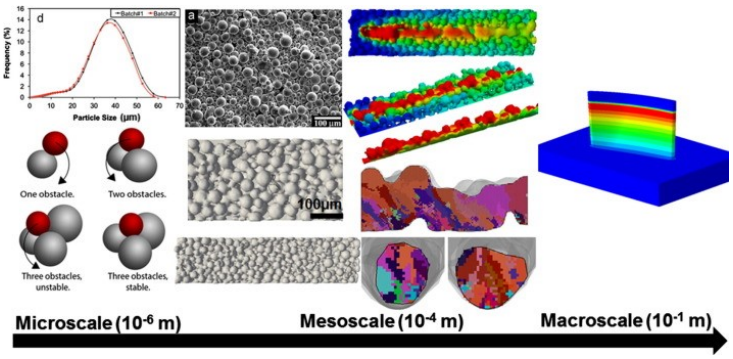

Figure 2.7: Schematic of approach scales to modelling of selective laser melting, reproduced from [40].

Similarly, the vast majority of the published studies were using the heat flux load to model the heat source, which often follows a Gaussian intensity distribution [41,42]. In addition to the Gaussian distribution, the heat flux source can be represented by a single element with the equal size of the beam diameter [43], or a constant power density instead [44]. Apart from the heat flux load, another way of modelling the heat source is directly applying a temperature load [45].

In addition, effective thermophysical parameters are utilized in the continuum models. Especially for porous structures such as lattice materials, some temperature-dependent parameters, such as thermal conductivity, specific heat capacity and density, are different from those of the bulk material. In order to simplify the problem, a number of studies considered constant thermophysical parameters during the SLM process [46,47]. Other studies used different thermophysical parameters for the powder and the solid component separately [43], or consider the thermophysical parameters changing with temperature on the basis of a simplified relation [48]. For instance, in terms of the porosity of the powder, the effective thermal conductivity is interpolated by using functions between zero and the bulk material value [49]. Similarly, specific heat can be calculated by linear interpolation or extrapolation and used as a pre-defined value [50].

As a matter of fact, FE method is the most commonly used techique to solve the continuum models for SLM. To model the growing parts during SLM, a special technique so-called Element birth and death technique, as schematically depicted in Figure 2.8, is introduced in many asscociated studies [51,52]. Specifically, this technique consists of three steps. First, the geometry model in-

cluding powder bed is converted to a finite element model. Then, all the generated elements are deactivated to ensure they have approximated zero contribution to thermal conductivity. Finally, when the laser starts to scan a certain layer, all the elements in this layer is activated. These steps are repeated until a complete building process is simulated.

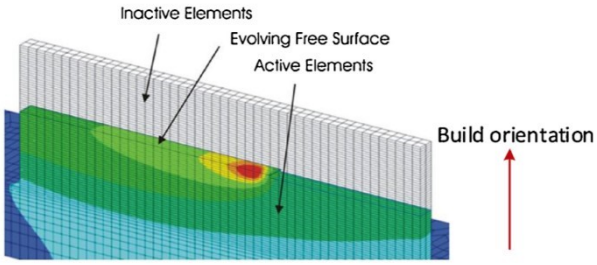

Figure 2.8: Graphical description of Element birth and death technique, reproduced from [51]. The gray region indicats the inactive element whilst colorful elements are active.

The continuum approaches are applicable for building thermal models or thermo-mechanical models for SLM process. Specifically, using a continuum thermal process model can predict the transient temperature of a part whilst it being built by SLM, which is crucial for determining the thermal stress and predicting the residual stress and distortion [48]. Over the years, massive studies have focused on the effects of the number of layers and the process parameters on the thermal response during a SLM process. Roberts [48] was simulate the temperature fields of a component during SLM and was observe that the first consolidated layer from titanium powder bed has a lower conductivity than the steel base plate. It follows, therefore, the upper layers retain the heat from the laser source, and experienced a slight but steady rise when the number of layers increased. Furthermore, the effects of the process parameters on the temperature field characteristics that was evaluated in lots of studies including the following points [53,54,55],

- The maximum temperature of a build part increases with higher laser power.
- The maximum temperature of a build part increases with lower scanning speed.
- The cooling rate decreases with higher laser power due to the smaller melt pool.

Apart from the temperature field, understanding the thermomechanical response also plays an importance role in predicting the quality of a SLM-processed part. Thermally induced residual stress and distortion affect strongly the mechanical performance and may attribute to dimensional inaccuracy to the produced part. A number of studies were develop a continuum mechanical model coupled to a thermal model to determine the influences of process parameters on the mechanical properties such as residual stresses and distortion [56,57]. The thermomechanical model and corresponding mechanical results are not the problems of interest in this work, so further details are not involved in this thesis.

3

PART-SCALE THERMAL MODELLING BASED ON MOVING GRID METHOD

IN this section, a moving grid model in part-scale is presented for the thermal analysis of lattice structures manufactured by SLM process. The model consists of two parts: a geometric model to import the architecture of a lattice structure of interest; a thermal model to simulate the thermal process of the designed lattice structure described by the geometric model. The thermal model is mainly developed based on a technique so-called moving grid method, which was mentioned in Guduru's work [19]. In contrast to the common modelling technique used in continuum models for SLM process, the element birth and death technique, the moving grid method uses a constant number of grid points to discretize a building component while the element birth and death technique introduces new activated elements for the new layer. This method has significant benefits of effectively investigate the transient thermal evolution of a lattice structure during SLM. Accordingly, the effects of process parameters in combination with the choice of the lattice architecture, on the thermal evolution can be evaluated. Further details of how to develop the geometric model and the thermal model are given in the following sections.

3.1. GEOMETRIC MODEL FOR LATTICE STRUCTURES

THE architecture of a lattice is one of the important factors that strongly influence its thermal evolution and mechanical performance. To simulate the thermal process of a lattice structure whilst it being built by SLM, first of all the expected architecture of this lattice structure is numerically described by designing a geometric model. After that, the construction of the lattice of interest is traceable and its thermal evolution during SLM can be modelled by a thermal model. It is known that a lattice is composed of repeated unit cells and each unit cell consists of several nodes and sets of struts connecting to the nodes. Accordingly, a geometric model for a lattice structure is generated in terms of two main steps: firstly figure the configuration of the unit cell, secondly define the arrangement of the repeated unit cells. Specifically, the configuration of a unit cell is represented on the basis of the positions of the connection nodes of their constituent struts, and element-node connectivity. Herein the connectivity is defined as the number of struts connecting at a node. Next, by defining the unit cell arrangement, for instance, the numbers of repeated unit cells in the axial and longitudinal direction separately, the architecture of a lattice structure is numerically described by this 2D geometric model.

With the purpose to evaluate the effect of the architecture of lattices on their thermal evolution during SLM, different 2D lattice models are generated by defining the geometric model. Herein the minimum cell of a lattice structure is defined as its elementary cell. Three kinds of lattice structures are inverstigated in this work and they are classified according to the shape of their elementary cells: triangular lattices, square lattices, and hexagonal lattices. The corresponding elementary cells for the lattices of interest are schematically listed in Table 3.1. Note that for a lattice structure, its elementary cell might be different from its unit cell as the elementary cell no need to be the minimum repeated unit for a lattice. For example, the elementary cell for a triangular lattice is exactly a triangle while its unit cell has a hexagonal shape as given in Figure 3.1(a).

To investigate the relationship between thermal evolution and the elementary cell shape, the lattice structures used for comparison are all having the same overall size as given in Figure 3.1 (b). In our work, each strut is assumed to be square cross-section and has a width w as depicted in Table 3.1, which is selected as a typical value of 0.5 mm. It is further assumed that a lattice structure is constructed by identical struts, where the cross-sectional width w is uniform for all the lattice members. For a better comparison, herein a typical width of all the elementary cells are selected as 4 mm. In other words, the strut length of triangular elementary cell, square elementary cell, and hexagonal elementary cell are 4 mm, 4 mm, and 2 mm, respectively.

Table 3.1: Schematic of the elementary cells of triangular lattice, square lattice, and hexagonal lattice. The primary physical difference between them is the number of nodal connectivity $Z = 6$ for triangular lattice, $Z = 4$ for square lattice, and $Z = 3$ for hexagonal lattice. The nodal connectivity Z describing the number of struts connecting at a node

Category	Elementary Cell	Nodal Connectivity	Strut Cross-sectional Dimensions
Triangular lattice	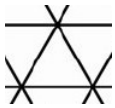	Z=6	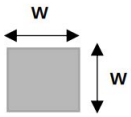
Square lattice	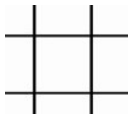	Z=4	
Hexagonal lattice	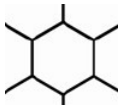	Z=2	

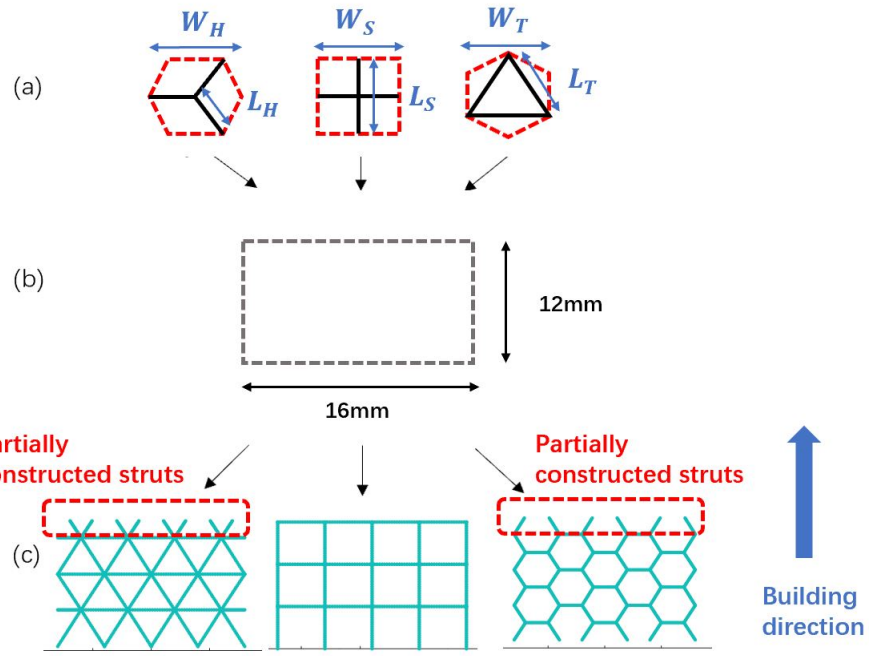

Figure 3.1: Schematic of how the 2D models for a triangular lattice, a square lattice, and a hexagonal lattice are generated. (a) gives the 2D configurations of these three unit cells, and L_T, L_S, L_H represent their strut length, respectively. The red dash lines draw the unit cell shape and black lines indicate the lattice struts, (b) is the chosen size for lattices of interest when modelling their thermal process during SLM, (c) schematically shows the three types of lattice structures with dimensions given in (b).

It is remarkable that the modelled lattice struts can be partially constructed and fully constructed. For example, a strut of the triangular lattice is so-called fully constructed if it has a length L_T equals to 4 mm. On the contrary, when the strut length is less than 4 mm, such strut is partially constructed as depicted in 3.1(c).

3.2. THERMAL MODEL DESCRIPTION

RECALL that, in SLM process, lattice members are created by selectively consolidating powder material in specific regions in the light of its architecture designed. To be more detailed, the laser beam applies the heat to the region of interest. In contrast, if no geometry exists in the underlying region, the heat source will be inactivated [53]. The consolidation is achieved by melting and subsequently cooling the powder in a single building layer, and this phenomenon is repeated in a layer-by-layer manner during SLM. In the real process, the scanning pattern in a building layer could be complex, in especial a high-fidelity scanning strategy during the simulation work might lead to a large computational cost [58]. Fortunately, each powder layer is regarded as a continuum in a part-scale modelling approach for SLM process. That is to say, the metallic powder in the current layer is modelled to be consolidated simultaneously and no need to take the specific scanning strategy into account. Accordingly, the computational efficiency of the part-scale thermal model can be dramatically enhanced.

In general, a complete SLM process requires numerous powder layers to finish a component. Consequently, the simulation of the SLM process consists of numerous heating and cooling cycles, and this leads to an enormous computational cost. Until now, most of the modelling approaches for SLM focus on the modelling of bulk materials with relatively simple geometries. However, this work is aiming to predict the temperature evolution of the members of a lattice. In our case, first of all the thermal process of every lattice strut are chosen to be modelled individually. Figure 3.2 shows the printing process of a hexagonal lattice during SLM. Obviously, only the struts on the top, which indicated as red bars in Figure 3.2, are growing with time in their length. Therefore, they are referred to as growing struts in this work. In contrast, other strut members with blue color are stationary with time, herein we call them stationary struts. Consequently, the lattice members can be classified in the light of their state. Specifically, stationary struts if they are fully constructed, and growing struts if they are still under construction.

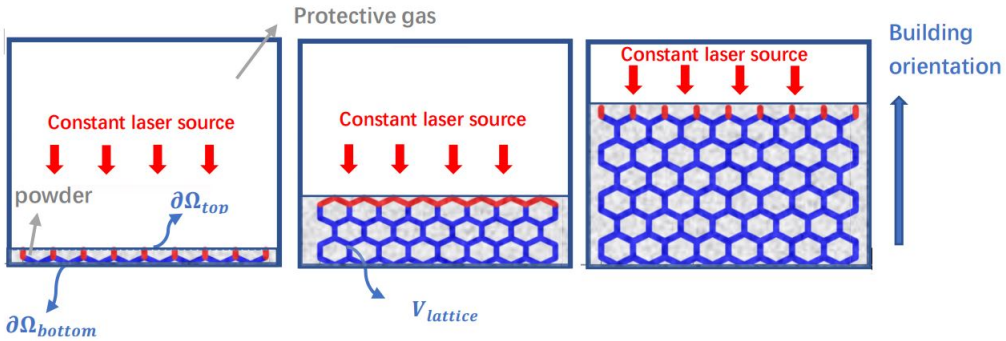

Figure 3.2: Printing process of lattice structure during SLM. The gray regions indicate the metal powders between the build solid lattice part. Protective gas is filling in the chamber during the printing process. Herein the space of the building lattice is divided into two boundaries and one domain: the top surface $\partial\Omega_{\text{top}}$, the bottom surface $\partial\Omega_{\text{bottom}}$, the space between the top and bottom surface V_{lattice}.

When a strut is growing, the conventional way to model its multiple layers construction is the Element birth and death technique. As introduced in the early chapter, this FE method usually

meshes a component by elements with equal and constant size [51,52]. Initially, the thermal conductivity matrix is multiplied with a very small number to deactivate all the elements. Once a layer is built, the elements within that layer will be activated by returning to their original conductivity values, so they could have contribution to the heat transfer process. Note that the activated elements will maintain to be active in the subsequent modelling. Accordingly, the number of active elements increases with time due to new layers are continuously processed. In other words, the conductivity matrix of this FE thermal model has a larger size when new elements are introduced, which causes a higher number of DOFs and a larger computational cost.

Instead of the element birth and death technique, an alternative approach so-called moving grid method, is applied in our thermal model to address the temperature evolution of lattice members whilst they being built by SLM. Firstly, a simple one-dimensional example is illustrated for a better explanation. Consider now a single strut member is growing from an initial length l_0 with a velocity $\dot{l}$ in the building direction. In this study, it is assumed that the slender struts are idealized to have a perfectly square cross-section along their length and thus a single strut can be considered as a 1D model. As schematically demonstrated in Figure 3.3, this 1D strut model is spatially discretized with equidistant grid points and the number of grid points is fixed. In this case, the length growth of a strut is addressed by an increased spatial interval between grid points, while the number of the grid points, in other works, the DOFs remains the same. Compared with the element birth and death technique, the moving grid method provides a higher computational efficiency as it no need to increase the number of DOFs to model the increased length of the building strut.

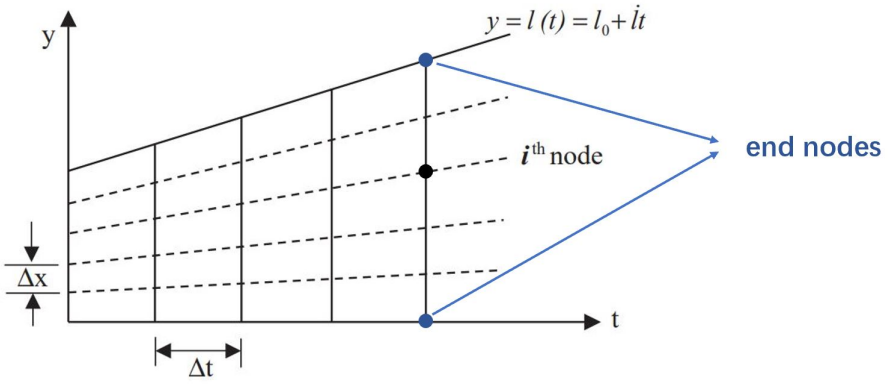

Figure 3.3: Moving space grid method to solve stress evolution equations, reproduced from [19]. The number of grid points is kept constant. However, the coordinate of i^{th} node moves with a velocity proportional to growth velocity $\dot{l}$.

Typically, a lattice structure is composed of lots of struts with varying orientations. The essential idea of the moving grid model for a lattice consists of two stages: firstly, each strut is modelled in 1D domain individually; secondly, applying the boundary conditions on the intersections between struts to integrally model the struts together due to they are all located in the same 2D plane. Note that the intersections are termed as the end nodes for the connecting struts as indicated in Figure **??**. In other words, a single strut is a 1D model while a lattice model can be expanded to 2D domain. Note that, several assumptions are required before applying the moving grid method to the 1D model for every lattice strut. First, it is assumed that each strut has an initial length l_0 and will grow to its full-length state L. For the first constructed layer of a lattice component, consider now the struts involved in this first layer, herein their initial length could be considered as the length of the base plate during the real SLM process. However, not all the struts are in contact with the base plate, and grow from an initial length is not the practical case for these struts. Therefore, a typical powder layer thickness for SLM, 50 μm, is chosen as the initial length l_0 in this work. Compared

with the size of a single lattice strut, such negelctable value makes the assumption associated with the inital length become applicable. Second, our thermal model further assumes that the temperature field at the strut cross-section is uniform, and all the struts have a temperature T_0 equals to their melting point T_m in the inital state of the simulated temperature evolution. Third, during the heating stage, heat radiation and heat convection are neglected in our thermal model for problem simplification. Fourth, for both heating and cooling stage, the thermal properties, including thermal conductivity k and convective heat transfer coefficient h_c, are assumed to be temperature independent. Last, the effect of phase change and heat loss by vaporization are ignored.

Based on the assumptions stated above, the temperature evolution along each 1D strut model is achievable by using the moving grid method in combination with a one-dimensional heat transfer equation,

$$\frac{\partial T}{\partial t} = \alpha \nabla^2 T = \alpha \left(\frac{\partial^2 T}{\partial y^2} \right), \tag{3.1}$$

where T is the temperature field, t is the time, y is the position in direction of the strut orientation, and α is the thermal diffusivity. Recall that a strut is growing from l_0 to its fully constructed length with a velocity $\dot{l}$ during SLM. In the meantime, the constant number of grid points continuously move with the same speed in the growing strut as depicted in Figure 3.3. Accordingly, the movement of node i during the heating process, as labelled in Figure 3.3, can be expressed as,

$$\left(\frac{\partial y}{\partial t} \right)_i = \left(\frac{\partial y}{\partial l} \right)_i \frac{\partial l}{\partial t} = \frac{y_i}{l} \dot{l}. \tag{3.2}$$

For node i, its temperature field T_i on node i depends on both its coordinate y_i and time t; the nodal position y_i depends on both the time t and the strut length in the current state $l(t)$. Accordingly, Eq 3.2 can be re-written as,

$$\frac{\partial T\left(y\left(l\left(t\right)\right), t\right)}{\partial t}_i = \alpha \left(\frac{\partial^2 T}{\partial y^2} \right)_y + \left(\frac{\partial y}{\partial t} \right)_i \left(\frac{\partial T}{\partial y} \right)_t, \tag{3.3}$$

$$\left(\frac{\partial T}{\partial t} \right)_i = \alpha \left(\frac{\partial^2 T}{\partial y^2} \right)_y + \left(\frac{\partial T}{\partial y} \right)_t \frac{y_i}{l} \dot{l}. \tag{3.4}$$

The above Eq 3.4 is the governing equation for temperature field evolution of a growing strut in the heating stage. In contrast, for stationary struts, they stop growing while the heat conduction continuously occur. Therefore, the growth rate $\dot{l}$ equals to zero for struts in these two states. Therefore, the governing equation for a stationary strut, or a growing strut in the cooling stage is given by,

$$\left(\frac{\partial T}{\partial t} \right)_i = \alpha \left(\frac{\partial^2 T}{\partial y^2} \right)_y. \tag{3.5}$$

Note that y is the position of node i in the orientation of the strut of interest. Eq 3.4 and Eq 3.5 are applied to a single strut member during the heating stage and cooling stage, respectively. However, lattices often have intricate geometry and are composed of numerous struts with varing orientations with respect to the building direction. In general, the SLM is a layer-wise printing process and has a fixed building orientation during the whole printing process. In a building layer u, its printing speed $\dot{l}_u$ represents the growth rate of all the struts within this layer in the building direction. As the local coordinate term, y, in the Eq 3.4 and Eq 3.5, depends on the strut orientation φ as described in Figure 3.4. Thus, Eq 3.4 for strut 1 should be re-written as,

$$\dot{l}_{\text{eff}} = \frac{\dot{l}_u}{\sin\left(\varphi_1\right)}, \tag{3.6}$$

$$\left(\frac{\partial T}{\partial t}\right)_i = \alpha\left(\frac{\partial^2 T}{\partial y^2}\right)_y + \left(\frac{\partial T}{\partial y}\right)_t \frac{y_i}{l}\dot{l}_{\text{eff}}. \tag{3.7}$$

where φ_1 is the smallest angle between the strut 1 and the base plate as shown in Figure 3.4, $\dot{l}_{\text{eff}}$ gives the effective length growth rate in the direction of strut orientation.

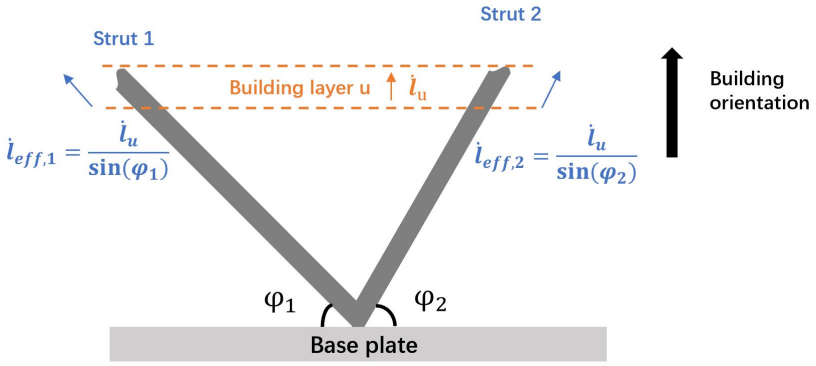

Figure 3.4: Schematic of simplified two struts model with different inclined angles φ_1 and φ_2, and the angle is defined as the smallest angle between the strut and the base plate. For the current building layer u with a printing speed $\dot{l}_u$, the strut 1 and strut 2 involved in this layer have the length growth rate $\dot{l}_{\text{eff},1}$ and $\dot{l}_{\text{eff},2}$, respectively. Such effective length growth is depending on the strut orientation.

Eq 3.7 and stated above is feasible for growing struts with various orientation except for a horizontal strut. It leads to an undefined result when φ=0 apply to Eq 3.7 due to having 0 in the denominator. As a horizontal strut is perpendicular to the printing direction, the metallic power is simultaneously consolidated to form the horizontal strut. In this case, the effective length growth rate in the horizontal direction is regarded as 0. Hence, the governing equation for a node i along a horizontal strut with a coordinate x in the horizontal direction is given as,

$$\left(\frac{\partial T}{\partial t}\right)_i = \alpha\left(\frac{\partial^2 T}{\partial x^2}\right)_x. \tag{3.8}$$

Different from another coordinate y representing the local coordinate in the direction the same as the orientation for an oblique strut, herein x defines another local coordinate for grid points of horizontal struts, and it is fixed in the horizontal direction. The above Eq 3.8 is applicable when a horizontal strut is stationary. For a horizontal strut is growing, its temeprature evolution should take the boundary conditions, such as the applied heat source, into account. Further details about the boundary conditions will be demonstrated in the next section.

3.2.1. BOUNDARY CONDITIONS

To define the boundary conditions of a 2D lattice structure whilst it being built by SLM, there are two surfaces and one domain to be discussed as depicted in Figure 3.5: the top surface $\partial\Omega_{\text{top}}$, the bottom surface $\partial\Omega_{\text{bottom}}$, the domain between the top and bottom surface V_{lattice}. For instance, during the heating stage of the SLM process, the boundary conditions of a typical 2D hexagonal lattice structure are clearly expressed in Figure 3.5. As for the heating case, the boundary conditions for the cooling stage are identical excepting for the top surface. Instead of a constant heat flux is applied by the laser beam during the heating stage, the heat loss occurs during the cooling stage due to the heat convection. Overall, the boundary conditions are summarized as following,

- A constant heat flux is applied on the top layer ($\partial\Omega_{\text{top}}$) during the heating stage.

- Heat loss occurs due to heat convection on the top layer ($\partial\Omega_{\text{top}}$) during the cooling stage.
- Temperature field on the bottom layer ($\partial\Omega_{\text{bottom}}$) connecting to the base plate equals to the air temperature T_0=300 K.
- No temperature gradient at the cross-sectional plane of each strut.

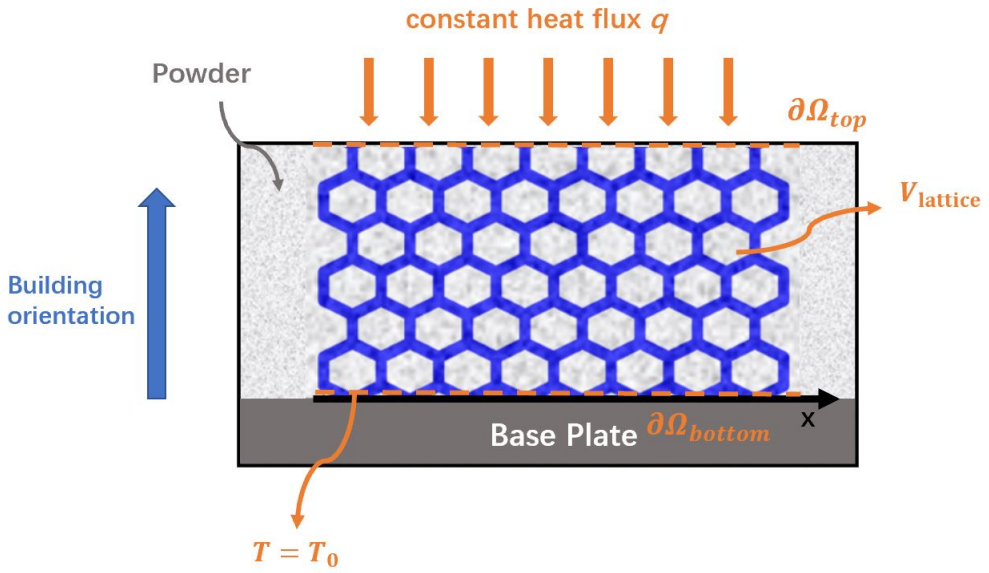

Figure 3.5: Description of thermal boundary conditions for a typical hexagonal lattice structure during SLM. The space of this 2D lattice model is divided into three sections: the top surface $\partial\Omega_{\text{top}}$, the bottom surface $\partial\Omega_{\text{bottom}}$, the domain between the top and bottom surface V_{lattice}. Herein x represents the axis in the horizontal direction.

In our moving grid model, first of all lattice members are modelled individually to determine their temperature evolution. Note that, when a moving grid method is applied to discretize the lattice members by a number of grid points, the boundary conditions stated before is prescribing the grid points on the both ends of each strut, which are the so-called end nodes as inidicated in Figure 3.2.

In fact, the boundary conditions of a strut are defined according to the location of its end nodes. Unlike the governing equations are separately stated in the previous section, herein the growing struts and the stationary struts are discussed together. We start with the bottom surface of the lattice $\partial\Omega_{\text{bottom}}$. A Dirichlet boundary condition can be used to prescribe the nodal temperature field if the grid point i on the bottom surface $\partial\Omega_{\text{bottom}}$ that contacting to the base plate,

$$T_i = T_0, \quad \text{on the surface } \partial\Omega_{\text{bottom}} \tag{3.9}$$

where T_0 is the initial temperature, which equals to the typical room temperature 300 K in our model. Besides, note that the strut end nodes are usually the intersection points between connecting lattice members. As the heat conduction between lattice members is continuously occuring during the SLM process, the boundary conditions of the intersection points locating between the top surface and the bottom surface, i.e., in the volume V_{lattice} labelled in Figure 3.2, can be defined in terms of the continuity of heat flow as following,

$$\rho c_p \frac{\partial T_i}{\partial t} = Q_{\text{conduction}}, \quad \text{in the space } V_{\text{lattice}} \tag{3.10}$$

where ρ is the density of the lattice material, c_p is the specific heat (at constant pressure), and $Q_{\text{conduction}}$ is the sum of generated heat energy per unit volume through the intersection point

of interest. For example, Figure 3.6 gives an intersection node i that connecting with three lattice members, and the total heat conduction from the neighboring nodes on the connected three struts through this boundary node i can be expressed as,

$$Q_{\text{conduction}}\, w = \sum_{n=0}^{3} q_n = \sum_{n=0}^{3} k \frac{T_n - T_i}{\Delta y_n}, \tag{3.11}$$

where w is the strut cross-sectional width, and Δy_n is the nodal distance between the intersection node i and the neighboring node on the connecting strut n. The term $Q_{\text{conduction}}$ in Eq 3.10 gives the total heat energy per unit volume of the lattice material due to thermal conduction. However, the term q_n in Eq 3.11 determines the contributions of all the struts connecting to node i to the heat conduction energy, which has the unit J/mm^2. Accordingly, a uniform strut width w is applied to transform the heat energy per unit area, q_n, to the volumetric heat energy $Q_{\text{conduction}}$. Thus, the lattice can be regarded as modelling in 3D space with a thickness of w in the direction perpendicular to the plane of the sampled lattice struts depicted in Figure 3.6.

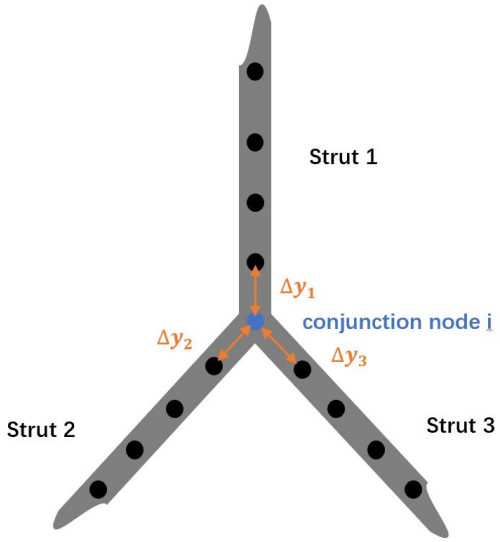

Figure 3.6: Schematic of an exampled conjunction node i that connecting with three struts: strut 1, strut 2, and strut 3. Herein only a portion of each struts is drawn in this figure, and such partial strut length is discretized by 5 grid points.

For a lattice during both the heating stage and the cooling stage, the boundary conditions for end nodes of each strut on the defined surface and space, $\partial\Omega_{\text{bottom}}$ and V_{lattice}, are identical whilst different on the top surface domain. During the heating process, a heat energy from the laser source is applied, meanwhile, heat conduction between lattice members continuously happens. Hence, the boundary condition for strut end nodes on domain $\partial\Omega_{\text{top}}$ is written as,

$$\rho c_p \frac{\partial T_i}{\partial t} = Q_{\text{conduction}} + Q_{\text{input}}, \quad \text{on the surface } \partial\Omega_{\text{top}}, \tag{3.12}$$

$$Q_{\text{input}} = \frac{\text{Power}}{Ad} \tag{3.13}$$

where Q_{input} represents the applied volumetric heat during the heating process to print a layer thickness material, A is the sum of the cross-sectional area of lattice members in a certain layer whilst it being printed by SLM. Figure 3.7 clearly demonstrates how the cross-sectional area A is defined.

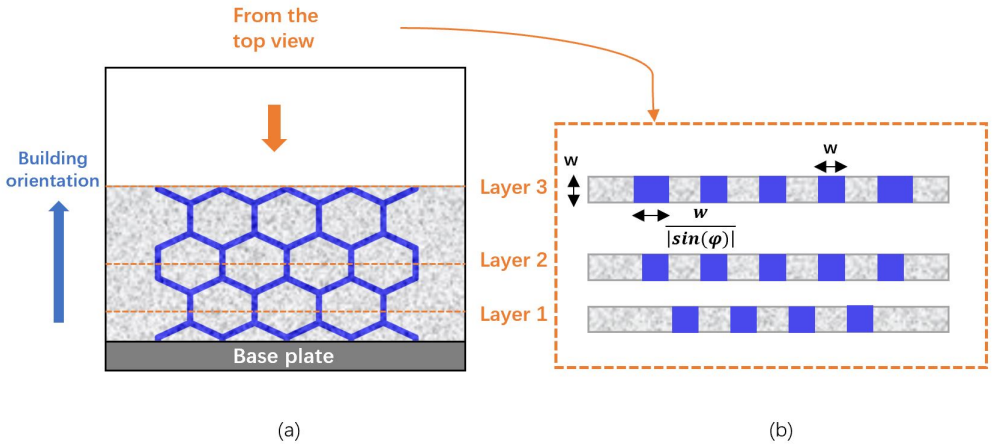

Figure 3.7: Schematic description of a hexagonal lattice structure whilst it being manufactured by SLM. (a) specify three power layers as the examples and their corresponding cross-sections are given in (b). In (b), the region of the strut cross-sections are indicated as the blue squares and rectangles for layer 1 to layer 3. It is assumed that all the lattice struts have an equal thickness w in the direction perpendicular to this 2D hexagonal lattice model. Note that the cross-sectional width of a single oblique strut depends on its orientation φ.

Similarly, during the cooling stage, heat loss due to convection replaces the heat flux input when the boundary nodes on the top surface $\partial\Omega_{\text{top}}$, thus Eq 3.12 can be re-written to,

$$\rho c_p \frac{\partial T_i}{\partial t} = Q_{\text{conduction}} + Q_{\text{convection}}, \quad \text{on the surface } \partial\Omega_{\text{top}}, \tag{3.14}$$

where $Q_{\text{convection}}$ defines the volumetric heat dissipation caused by convection between protective gas in the build chamber and the lattice material, and it is given as,

$$wQ_{\text{convection}} = h_c\,(T_e - T_i)\,, \tag{3.15}$$

where h_c is the heat transfer coefficient, T_e is the temperature of the protective gas which takes the value of 300K as the room temperature.

Recall that each 1D strut model is spatially discretized with grid points by using the moving grid method. The stated boundary conditions in this section is used for its two end nodes. For other grid points between the end nodes, so-called as central nodes, their temperature evolutions are determined by the governing equations mentioned in the previous section. Until now, the boundary conditions for strut end nodes in varying domains are derived. However, for a horizontal strut, it is possible that all the grid points are located on the boundary surfaces $\partial\Omega_{\text{top}}$ and $\partial\Omega_{\text{bottom}}$. The later case will not be considered in this work as it can be simplified as a part of the base plate. For the former, consider now a horizontal strut is exactly located on the top surface, and the position of its grid points is described by the coordinate in the horizontal direction, x. Herein the boundary conditions Eq 3.12 and Eq 3.14 are only for its two end nodes. Hence, the governing equation Eq 3.8 for the temperature evolution of its central nodes is re-written by taking the boundary conditions into account as followings,
during the heating process,

$$\left(\frac{\partial T}{\partial t}\right)_i = \alpha \left(\frac{\partial^2 T}{\partial x^2}\right)_x + \frac{Q_{\text{input}}}{\rho c_p}, \tag{3.16}$$

during the cooling stage:

$$\left(\frac{\partial T}{\partial t}\right)_i = \alpha \left(\frac{\partial^2 T}{\partial x^2}\right)_x + \frac{Q_{\text{convection}}}{\rho c_p}. \tag{3.17}$$

3.2.2. FRONT-FIXING SCHEME

THE moving grid method is an efficient technique to solving a moving domain problem by using a fixed number of grid points to discretize a growing domain. Recall that Figure 3.3 gives the discretization scheme for a 1D case when applying the moving grid method. Besides, Crank [59] presented a similar discretization scheme for 2D problem in the global coordinate, $x-y$ plane, which is so-call the Front-tracking approach and its scheme is shown in Figure 3.8(a). Herein the spatial intervals between grid points, Δx and Δy, are increase in response to the time domain. Alternatively, Crank stated another simplified discretization scheme on the basis of the Front-tracking scheme, which is so-called the Front-fixing scheme as described in Figure 3.8(b).

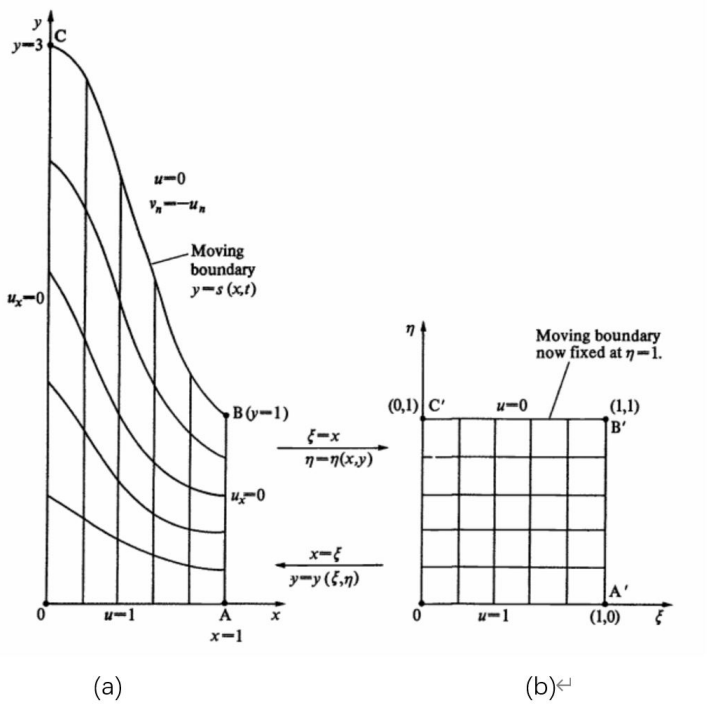

Figure 3.8: 2D physical plane and transformed plane, reproducted from [59]. (a) grids of Front-tracking scheme in $x-y$ plane. (b) grids of Front-fixed scheme in $\eta-\zeta$ plane. X is used to replace η in our model.

The basic idea of the transformation illustrated in Figure 3.8 is normalizing the coordinates x and y to be dimensionless coordinates ζ and η, which are both ranged from 0 to 1. Similarly, it also can be applied to simplify the 1D moving grid model. Recall that x is the local coordinate for a horizontal strut in the horizontal direction, while y refers to the local coordinate of a certain oblique strut in a direction consistent with its orientation. Based on the transformation as depicted in Figure 3.9, in this work we use X as the dimensionless coordinate of a horizontal strut and ranges from 0 to 1, meanwhile, ζ is the dimensionless form of the local coordinate y for an oblique strut model. Obviously, in Figure 3.9 (b), the coordinate of every grid point is constant in time.

Until now, the governing equations and boundary conditions for predicting temperature evolution of all the struts of a lattice are all prescribed by using the local coordinate y or x. To further simplify these equations, the Front-fixing scheme introduces some dimensionless transformations as follows,

$$\theta = \frac{T - T_0}{T_m - T_0}, \tag{3.18}$$

$$\tau = \frac{t\alpha}{l_0^2}, \tag{3.19}$$

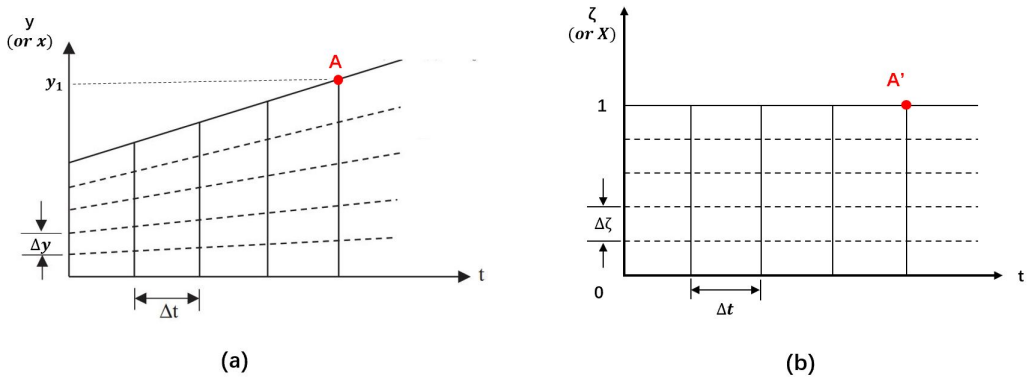

Figure 3.9: Schematic description of normalizing a single 1D strut model. (a) is the moving grid scheme for a single strut with the local coordinate y (or x), where the position of point A is $y_A = y_1$. (b) is the same discretization scheme but based on the Front-fixed approach transforming the local coordinate to ζ (or X) ranges from 0 to 1, where the position of point A is $\zeta_{A'} = 1$ for all instants in time.

$$H = \frac{l}{l_0}, \tag{3.20}$$

$$\frac{\partial H}{\partial \tau} = \dot{H} = \frac{\dot{l} l_0}{\alpha}, \tag{3.21}$$

$$\beta = \frac{l_0}{L}, \tag{3.22}$$

$$Bi = \frac{h_c l_0}{k}, \tag{3.23}$$

$$P = \frac{d\text{Power}}{Ak(T_m - T_0)}, \tag{3.24}$$

for an oblique strut,

$$Y = \frac{y}{l_0}, \tag{3.25}$$

$$\zeta = \frac{Y}{H}, \quad 0 \le \zeta \le 1, \tag{3.26}$$

for a horizontal strut,

$$X = \frac{x}{L}, \quad 0 \le X \le 1, \tag{3.27}$$

where T_m is the melting point depends on the lattice material, θ gives the dimensionless temperature field ranging from 0 to 1, τ is the dimensionless time. These dimensionless transformations could provide a comprehensive insight of evaluating the process parameters and conditions. H is a dimensionless parameter defining the relation between the transient length l for a strut with respect to its initial length l_0, Biot number Bi quantifies the thermal conductivity and the ability of thermal convection comprehensively, P is a dimensionless parameter that describes the heat input from the laser source.

For the purpose of explaining the specific application of the Front-fixed approach on modelling the thermal evolution on a lattice member, Figure 3.10 gives an example when the Front-fixing scheme is applying on a vertical lattice strut. It is worth noting that, for the same grid point, its local coordinate is consistent from non-dimensional time steps τ_j to τ_{j+1}. Specifically, ζ=0 is the coordinate of the bottom end node for the vertical strut in both time steps τ_j and τ_{j+1}. Similarly, ζ=1 denotes its top end node. The dimensionless parameter X plays in the same role for a horizontal strut. To simulate the thermal evolution of a lattice strut, the boundary conditions are

prescribed when $\zeta(or X)$ has a value of 0 or 1 (i.e., the end nodes). Besides, for $\zeta(or X)$ ranges between 0 and 1 (exclusive of 0 and 1), the governing equations are applied.

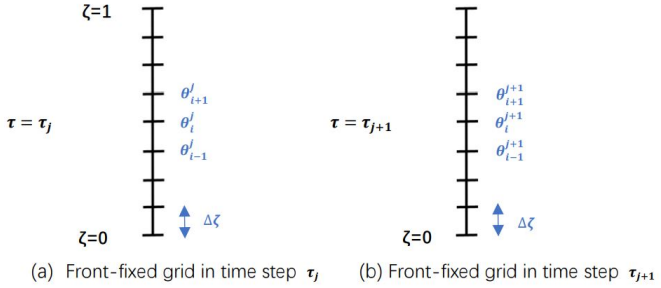

(a) Front-fixed grid in time step τ_j (b) Front-fixed grid in time step τ_{j+1}

Figure 3.10: Description for 1D finite difference grid based on the Front-fixing approach from dimensionless time step τ_j (a) to τ_{j+1} (b).

Therefore, the temperature evolution for each lattice strut could be addressed with the normalized coordinate ζ for an oblique strut or X for a horizontal strut. We start from an oblique strut growing in the heating stage of SLM process. The governing equation, Eq 3.4, is re-written as,

$$\frac{\partial\theta}{\partial\tau} = \left(\frac{\partial^2\theta}{\partial\zeta^2}\right)_\zeta \frac{1}{H^2} + \left(\frac{\partial\theta}{\partial\zeta}\right)_\zeta \dot{H}\frac{\zeta}{H}, \tag{3.28}$$

with the normalized boundary conditions,

$$\theta = 0, \quad \text{on the surface } \partial\Omega_{\text{bottom}}, \tag{3.29}$$

$$\frac{\partial\theta}{\partial\tau} = Q_{\text{conduction}} + P, \quad \text{on the surface } \partial\Omega_{\text{top}}, \tag{3.30}$$

$$\frac{\partial\theta}{\partial\tau} = Q_{\text{conduction}}, \quad \text{in the volume } V_{\text{lattice}}. \tag{3.31}$$

The specific expression $Q_{\text{conduction}}$ will be re-written in the following section based on the dimensionless transformations listed above. Furthermore, for a stationary oblique strut, or an oblique strut during the cooling stage, the governing equation Eq 3.5 is modified as,

$$\frac{\partial\theta}{\partial\tau} = \left(\frac{\partial^2\theta}{\partial\zeta^2}\right)_\zeta \frac{1}{H^2}, \tag{3.32}$$

with the normalized boundary conditions,

$$\theta = 0, \quad \text{on the surface } \partial\Omega_{\text{bottom}}, \tag{3.33}$$

$$\frac{\partial\theta}{\partial\tau} = Q_{\text{conduction}} - \frac{Bil_0}{w}\theta, \quad \text{on the surface } \partial\Omega_{\text{top}}, \tag{3.34}$$

$$\frac{\partial\theta}{\partial\tau} = Q_{\text{conduction}}, \quad \text{in the volume } V_{\text{lattice}}. \tag{3.35}$$

Now consider a growing horizontal strut. Its governing equations, Eq 3.16 and Eq 3.17, for the heating state and the cooling stage are read as,
during the heating stage,

$$\frac{\partial\theta}{\partial\tau} = \left(\frac{\partial^2\theta}{\partial X^2}\right)_X \beta^2 + P, \tag{3.36}$$

with the normalized boundary conditions,

$$\frac{\partial\theta}{\partial\tau} = Q_{\text{conduction}} + P, \quad \text{on the surface } \partial\Omega_{\text{top}}, \tag{3.37}$$

during the cooling stage,

$$\frac{\partial\theta}{\partial\tau} = \left(\frac{\partial^2\theta}{\partial X^2}\right)_X \beta^2 - \frac{\beta Bi\theta}{\partial X}, \tag{3.38}$$

with the normalized boundary conditions,

$$\frac{\partial\theta}{\partial\tau} = Q_{\text{conduction}} - \frac{Bil_0}{w}\theta, \quad \text{on the surface } \partial\Omega_{\text{top}}, \tag{3.39}$$

Moreover, for a stationary horizontal strut, the corresponding governing equation Eq 3.8 is normalized to,

$$\frac{\partial\theta}{\partial\tau} = \left(\frac{\partial^2\theta}{\partial X^2}\right)_X \beta^2. \tag{3.40}$$

with the normalized boundary conditions,

$$\frac{\partial\theta}{\partial\tau} = Q_{\text{conduction}}, \quad \text{in the volume } V_{\text{lattice}}. \tag{3.41}$$

After obtaining the normalized governing equations and boundary conditions, the temperature evolution of lattice members can be solved by using the Finite difference approximation. Note that the normalization of the term $Q_{\text{conduction}}$ in boundary conditions is a complex problem and will be further detailed in the following section.

3.2.3. FINITE DIFFERENCE APPROXIMATION

FOR the aim of modelling the thermal process of a lattice whilst it being built by SLM, we could predict the temperature evolution of the lattice members by applying the finite difference approximation to solve the governing equations and boundary conditions normalized in the previous section. To better explain the basic idea of the Finite difference approximation, we start with a 1D case. When we consider the lattice members individually, every single strut is modelled as a 1D domain and is discretized by grid points with equal size Δx. Figure 3.11 zooms in to three of the grid points, which are node $m-1$, node m, and node $m+1$. In this case, the finite difference approximation is used to solve the temperature change rate on the node m. Accordingly, it is known that the 1^{st} and 2^{nd} derivatives of the temperature field on node m are centrally approximated in space as,

$$\frac{\partial T}{\partial x}|_m = \frac{T_{m+1} - T_{m-1}}{2\Delta x}, \tag{3.42}$$

$$\frac{\partial^2 T}{\partial x^2}|_m \simeq \frac{T_{m+1} - 2T_m + T_{m-1}}{\Delta x^2}, \tag{3.43}$$

Consider now the moving grid model for a lattice based on the Front-fixing scheme. To approximate the temperature evolution on the grid points of a single strut model as given in Figure 3.10, the finite difference equation centered in space forward in time rewrites the governing equations derived in the previous section as,
for an oblique strut in the growing domain during the heating process,

$$\theta_i^{j+1} - \theta_i^j = \frac{\Delta\tau}{\Delta\zeta^2 H^2}\left(\theta_{i+1}^j - 2\theta_i^j + \theta_{i-1}^j\right) + \dot{H}\frac{\zeta\Delta\tau}{2\Delta\zeta H}\left(\theta_{i+1}^j - \theta_{i-1}^j\right), \tag{3.44}$$

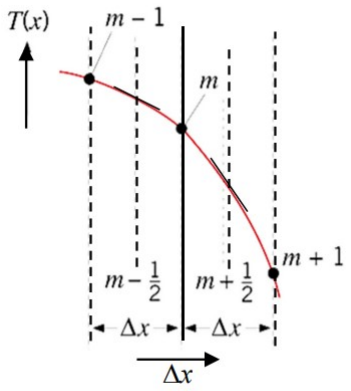

Figure 3.11: Schematic description of a 1D finite difference scheme. The nodal distance equals to Δx in the horizontal direction. The temperature derivatives at points can be approximated by the finite difference method

for a stationary oblique strut, or a growing oblique strut during the cooling stage,

$$\theta_i^{j+1} - \theta_i^j = \frac{\Delta\tau}{\Delta\zeta^2 H^2}\left(\theta_{i+1}^j - 2\theta_i^j + \theta_{i-1}^j\right), \tag{3.45}$$

for a horizontal strut in the growing domain during the heating stage,

$$\theta_i^{j+1} - \theta_i^j = \frac{\beta^2\Delta\tau}{\Delta X^2}\left(\theta_{i+1}^j - 2\theta_i^j + \theta_{i-1}^j\right) + P\Delta\tau, \tag{3.46}$$

for a horizontal strut in the growing domain during the cooling stage,

$$\theta_i^{j+1} - \theta_i^j = \frac{\beta^2\Delta\tau}{\Delta X^2}\left(\theta_{i+1}^j - 2\theta_i^j + \theta_{i-1}^j\right) - \frac{\theta_i^j \beta Bi}{\Delta X}\Delta\tau, \tag{3.47}$$

for a stationary horizontal strut,

$$\theta_i^{j+1} - \theta_i^j = \frac{\beta^2\Delta\tau}{\Delta X^2}\left(\theta_{i+1}^j - 2\theta_i^j + \theta_{i-1}^j\right). \tag{3.48}$$

However, the lattice structure is placed in a 2D plane, and the connectivity of the intersection points between struts needs to be taken into account. Note that an intersection point must be the end nodes of connecting struts. Herein the thermal evolution on an intersection point could be determined according to the prescribed boundary conditions, and it is no longer a 1D problem since the heat transfer due to thermal conduction between connecting struts in different direction is considered now. Therefore, a 2D finite difference approximation is required for addressing the boundary conditions.

Typically, such 2D finite difference approach is applied for a bulk material. To better explain how the 2D finite difference approach works on a lattice model, we start with a simpler case, which is the generalized 2D finite difference grid for a square bulk material as schematically shown in Figure 3.12(a). Herein an interior node(m,n) of interest (indicated in Figure 3.12 (b)) and its neighboring nodes are zoomed in as shown in Figure 3.12(b). For the unsteady-state case, where the temperature will change in the time domain. To determine the total thermal conduction energy $Q_{conduction}$ through the node(m,n) in a certain time step t_j, a fictitious element associated with this node is defined as the pink region indicated in Figure 3.12(b). It is worth noting that the nodal element region is restricted by half of the distance between it and the neighboring nodes, so the

highlighted element of node(m,n) has a dimension of $\Delta x \times \Delta y$. Accordingly, the sum of the volumetric heat energy $Q_{\text{conduction}}$ on node(m,n) due to thermal conduction is expressed as,

$$Q^{j}_{\text{conduction}}\Delta x\Delta y = \Delta y q^{j}_{m-1,n\to m,n} + \Delta y q^{j}_{m+1,n\to m,n} + \Delta x q^{j}_{m,n-1\to m,n} + \Delta x q^{j}_{m,n+1\to m,n}, \tag{3.49}$$

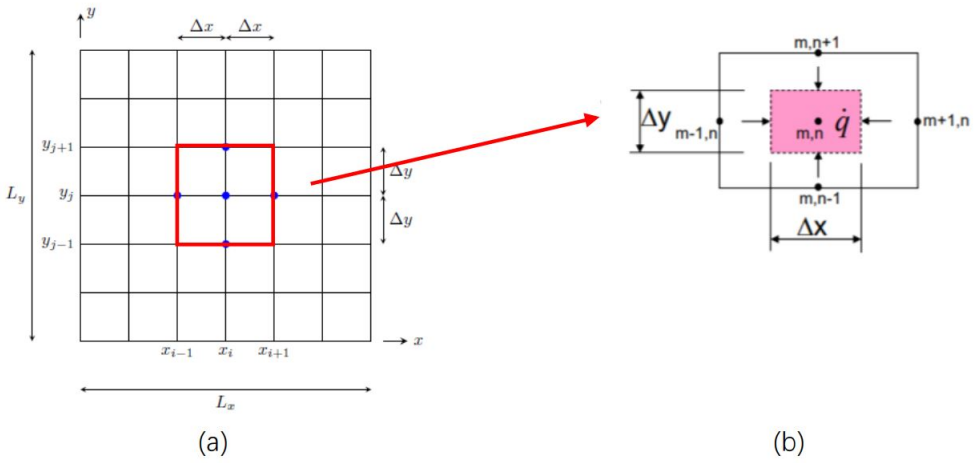

Figure 3.12: Description of 2D finite difference grid in time step t_j (a) is the overall scheme for 2D elements in $x-y$ space (b) focus a center node(m,n) and the element associated with it. The neighboring nodes of node(m,n) are indicated as well. Element area of node(m,n) are defined by the pink region with width Δx and length Δy.

where $q^{j}_{1\to 2}$ defines the heat flux from point 1 to point 2 in the time step j. Usually, it is easy to figure out the element area associated with the node of interest is for a bulk material. However, it becomes a significant challenge for the intersection points of a lattice structure. Following a similar idea to define the element associated with the intersection points of a lattice material, the resulted element region might have irregular shapes. For instance, Figure 3.13 demonstrates two examples of the conjunction nodes of a lattice and highlights their element region in a green color.

In Figure 3.13(a) (b), the elements associated with the intersection points indicated as the green regions are irregular shapes. The complex geometry of them makes it difficult to measure the element area. To address that, an assumption is stated in our model that the element area of an intersection point of interest has a fixed dimension of $w \times w$, where w is the width of all the lattice members. For instance, the highlighted regions with pink color in Figure 3.13(c) (d) are describing the new defined elements in terms of this assumption. This assumption will introduce more error but remarkably simplify the problem.

Similar with the Eq 3.49, the energy balance equations with the boundary conditions specified in the previous Section 4.2.1 can be derived. Eventually, by using the simplified finite difference approximation, the normalized equation for an end node i in different domains are re-written to,

$$Q_{\text{total}}\,w^2 = Q_{\text{conduction}}\,w^2 = \sum_{n=0} q_n w + \sum_{m=0} q_m w, \tag{3.50}$$

$$\theta_i^{j+1} - \theta_i^{j} = \frac{l_0 \Delta\tau}{w}\left(\sum_{n=0}\frac{\theta_n^j - \theta_i^j}{H_n \Delta\zeta_n} + \sum_{m=0}\beta\frac{\theta_m^j - \theta_i^j}{\Delta X_m}\right), \quad \text{in the volume } V_{\text{lattice}}, \tag{3.51}$$

during the heating stage,

$$Q_{\text{total}}\,w^2 = Q_{\text{conduction}}\,w^2 + Q_{\text{input}}\,w^2 = \sum_{n=0} q_n w + \sum_{m=0} q_m w + \frac{P\,(T_m - T_0)\,k}{l_0^2}\,w^2, \tag{3.52}$$

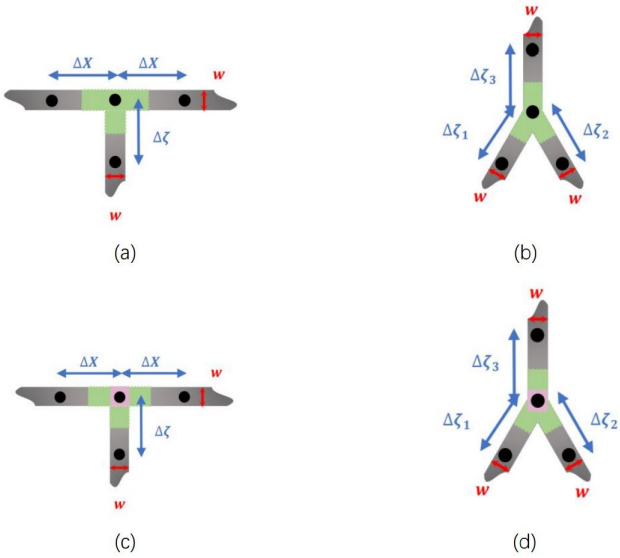

Figure 3.13: Description of two approaches to define the conjunction grid. Two types of the lattice struts models are used for the demonstration. (a) and (b) are illustrating how a conjunction element can be defined by following the 2D generalized Finite difference approach. The green regions are indicating the element area associated with the conjunction node of interest. (c) and (d) using the pink regions alternatively to represent the conjunction element for the problem simplification.

$$\theta_i^{j+1} - \theta_i^j = \frac{l_0 \Delta\tau}{w}\left(\sum_{n=0} \frac{\theta_n^j - \theta_i^j}{H_n \Delta\zeta_n} + \sum_{m=0} \beta \frac{\theta_m^j - \theta_i^j}{\Delta X_m}\right) + P\Delta\tau, \quad \text{on the surface } \Omega_{\text{top}}, \tag{3.53}$$

during the cooling stage,

$$Q_{\text{total}}\, w^2 = Q_{\text{conduction}}\, w^2 + Q_{\text{input}}\, w^2 = \sum_{n=0} q_n w + \sum_{m=0} q_m w + h_c\,(T_0 - T)\, w, \tag{3.54}$$

$$\theta_i^{j+1} - \theta_i^j = \frac{l_0 \Delta\tau}{w}\left(\sum_{n=0} \frac{\theta_n^j - \theta_i^j}{H_n \Delta\zeta_n} + \sum_{m=0} \beta \frac{\theta_m^j - \theta_i^j}{\Delta X_m} - Bi\theta_i^j\right), \quad \text{on the surface } \Omega_{\text{top}}, \tag{3.55}$$

where n numbers the oblique struts connecting on the intersection point i while m refers to the connected horizontal struts.

In fact, the strut orientation is neglected based on our assumption. A special case should be noted is when the connectivity of a boundary node equals to 1, i.e., it not the conjunction between lattice members. Its boundary condition can be prescribed in a similar way but need to consider the contribution of the orientation of the strut that the simulation focusing on. Figure 3.14 demonstrates that the heat transfer on the surface Ω_{top} will pass through an effective width of a single strut, and this effective width depends on the strut angle φ. Therefore, the nodal boundary conditions in this case are given as,
during the heating stage,

$$\theta_i^{j+1} - \theta_i^j = \frac{l_0 \Delta\tau}{w}\left(\sum_{n=0} \frac{\theta_n^j - \theta_i^j}{H_n \Delta\zeta_n} + \sum_{m=0} \beta \frac{\theta_m^j - \theta_i^j}{\Delta X_m} + \frac{P}{sin(\phi)}\right), \quad \text{on the surface } \Omega_{\text{top}}, \tag{3.56}$$

during the cooling stage,

$$\theta_i^{j+1} - \theta_i^j = \frac{l_0 \Delta\tau}{w}\left(\sum_{n=0} \frac{\theta_n^j - \theta_i^j}{H_n \Delta\zeta_n} + \sum_{m=0} \beta \frac{\theta_m^j - \theta_i^j}{\Delta X_m} - \frac{Bi\theta_i^j}{sin(\phi)}\right), \quad \text{on the surface } \Omega_{\text{top}}, \tag{3.57}$$

where φ gives the angle of the concerned strut with respects to the horizontal direction.

Besides, for the case that an end node has connectivity of 1 and located inside the lattice volume domain V_{lattice}, we apply adiabatic condition on this node thus prescribed as:
for oblique struts:

$$grad\theta \cdot \boldsymbol{\zeta} = 0, \tag{3.58}$$

$$\theta_i = \theta_n, \quad \text{in the volume } V_{\text{lattice}}, \tag{3.59}$$

for horizontal struts:

$$grad\theta \cdot \boldsymbol{X} = 0, \tag{3.60}$$

$$\theta_i = \theta_m, \quad \text{in the volume } V_{\text{lattice}}. \tag{3.61}$$

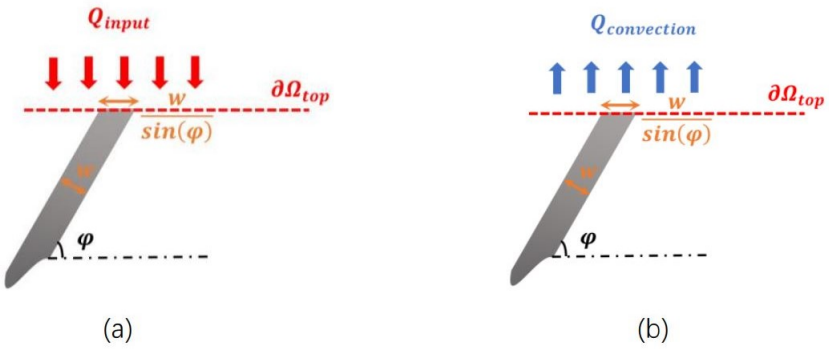

Figure 3.14: Description of the effective strut width on the top surface for an oblique strut with inclined angle φ. (a) demonstrating the strut is under the heating source melting with the constant energy input Q_{input}. (b) representing the strut during the cooling process that heat dissipation due to heat convection $Q_{\text{convection}}$] occurring.

3.2.4. STABILITY CONDITION

It is well known that finite difference method is a common technique for approximating the solution at a finite number of grid points in the domain. Once a finite difference formula has been established, the question that arises naturally is whether such approximation is stable. Stability analysis is the core to get convergence so that the results can be achievable. Consequently, the limit of allowable time step is investigated in this section.

T. M. A. K. Azad and L. S. Andallah [60] summarized the stability conditions for two standard finite difference schemes FTBSCS (forward time backward space and centered space) and FTCS (forward time and centered space), which are specified in Appendix B. Recall that the explicit finite difference approach applied in our thermal model for lattice materials follows the latter scheme (i.e. FTCS), and the corresponding stability conditions proposed in Appendix B are,

$$0 \leq \frac{2D\Delta t}{\Delta x^2} \leq 1, \quad \text{and} \quad 0 \leq \frac{u\Delta t}{\Delta x} \leq 2\left(1 - \frac{D\Delta t}{\Delta x^2}\right), \tag{3.62}$$

where the coefficients u and D are defined by the discretized finite difference equation:

$$\frac{c_i^{n+1} - c_i^n}{\Delta t} + u\frac{c_{i+1}^n - c_{i-1}^n}{2\Delta x} = D\frac{c_{i+1}^n - 2c_i^n + c_{i-1}^n}{\Delta x^2}. \tag{3.63}$$

Accordingly, for the oblique struts, the maximum limits of normalized time step $\Delta\tau$ for the governing equations of them can be expressed as,
for growing struts during the heating stage,

$$\Delta\tau \leq \frac{H^2\Delta\zeta^2}{2} \quad \text{and} \quad \Delta\tau \leq \frac{2H^2\Delta\zeta^2}{2-\dot{H}H\zeta\Delta\zeta}, \tag{3.64}$$

for growing struts during the cooling stage, or stationary struts in both heating stage and cooling stage,

$$\Delta\tau \leq \frac{H^2\Delta\zeta^2}{2}. \tag{3.65}$$

Furthermore, for the normalized governing equations of the horizontal struts, their stability conditions are altering to,

$$\Delta\tau \leq \frac{\Delta X^2}{2\beta^2}. \tag{3.66}$$

To summarized a feasible stability conditions for a lattice strut in all the cases, the determined stability conditions are compared. Eventually, it can be found Eq.3.66 providing a minimum limitation of the maximum normalized time step $\Delta\tau$.

3.2.5. PARAMETERS EVALUATION

PHYSICAL PARAMETERS

As stated in the early stage, the process parameters usually have significant influence on the thermal evolution of build lattices during SLM. Evaluating the efforts of process parameters is one of the aims in this paper. Among varying process parameters for SLM, this section mainly focuses on the laser power, build-up rate, and cooling conditions in the combination with the lattice architecture of interest.

The addition of powder material in layer based SLM process have presented challenges in creating a numerical model. In this work, a moving grid approach was introduced as the solution. It assumes all the lattice members are built from an initial length l_0. To simulate the real process as closely as possible, herein l_0 takes a negligible value of 50 μm, which is the typical layer thickness d as well. Consider now the heating process of SLM, the powder regions of interest that has depth d, are melted by the laser beam. After that, the laser source will stop, and the molten materials are solidified and cooled down during the cooling stage. It is well known that a SLM process requires enormous heating and cooling process cycles to finish a component. The build-up rate and the laser power and are the process parameters considered during the heating stage, while the cooling duration deals with the following cooling stage.

Start with the process parameters for the heating stage. It is known that the layer thickness d, scanning velocity v_s and scan line spacing Δy_s are the main influencing variables of primary process time for SLM. The process related build-up rate $\dot{V}$is directly defined as the product of these three variables,

$$\dot{V} = d \cdot v_s \cdot \Delta y_s. \tag{3.67}$$

Actually, scanning velocity v_s and layer thickness are limited by the range of laser power [61]. Numerous studies investigated the efforts of the power input on other process parameters and the final SLM products. Alternatively, we are using the parameter VED to establish the correlation between heat input and various process parameters in the light of the following equation,

$$VED = \frac{power}{d \cdot v_s \cdot \Delta y_s} = \frac{power}{\dot{V}}. \tag{3.68}$$

Accordingly, the parameter VED is exactly the ratio of the laser power to the volumetric build rate. By constraining the energy density VED, the corresponding laser power can be ensured when inputting a certain value of productivity. To quantify the contributions of VED and $\dot{V}$ on the resulted temperature field, varying values of them are evaluated in this work. Herein, the volumetric energy densities of 50 J/mm^3, 100 J/mm^3, 200 J/mm^3 and 300 J/mm^3 are chosen while the value of volumetric build rate used is in the range of 1 mm^3/s and 4 mm^3/s.

Based on the selected build-up rate $\dot{V}$, the length growth rate $\dot{l}$ of an imported lattice structure can be determined as,

$$\dot{l}_m = \frac{\dot{V}}{A_m}, \tag{3.69}$$

where A_m indicates the cross-sectional area for concerned regions on the powder layer m, which is schematically demonstrated in Figure 3.7. In this regard, the volumetric build rate is a constant value during the whole building process whilst the length growth rate depends on the printed layer of interest.

Note that the build rate is defaulted in the vertical direction, then the obtained $\dot{l}_m$ represents the growth rate in vertical direction as well. After that, in a building layer m, the processing time for the heating stage is expressed as,

$$t_{\mathrm{m,heating}} = \frac{d}{\dot{l}_m}. \tag{3.70}$$

Combine with the non-dimensional transformation of the time variable, Eq 3.19, the normalized time variable is,

$$\tau_{\mathrm{m,heating}} = \frac{A_m \alpha}{\dot{V} d}. \tag{3.71}$$

The term l_0 in Eq 3.18 is directly represented by a single layer thickness d. That is to say, with a constant time step $\Delta\tau$, the number of time step costed for the temperature evolution during different material layers is changed. At the same time, the expression of dimensionless parameter $\dot{H}$ Eq 3.21 is altered to,

$$\dot{H}_m = \frac{\dot{l}_m l_0}{\alpha}. \tag{3.72}$$

Likewise, the inclined angle is required to calculate the effective $\dot{H}_{\mathrm{m,eff}}$ for oblique struts. Recall that the transformation of another dimensionless parameter, P, is defined in terms of the cross-sectional area A_m in Eq 3.24. Hence, it can be re-written as,

$$P_m = \frac{power \cdot d}{A_m k (T_m - T_0)}. \tag{3.73}$$

Based on the equations stated above, the normalized variables associated with concerned process parameters are computable, thus the influence of build rate and energy density can be quantified.

Furthermore, another process parameter concerning during the cooling stage is the cooling duration. In our thermal model, a cooling stage is applied after every heating stage as assumed earlier. A new non-dimensional parameter λ is introduced herein to describe the ratio of the cooling duration for layer m with respect to the heating duration $\tau_{\mathrm{m,heating}}$,

$$\lambda = \frac{\tau_{\mathrm{m,cooling}}}{\tau_{\mathrm{m,heating}}}, \tag{3.74}$$

where $\tau_{\mathrm{m,heating}}$ calculate from Eq 3.71 is the costed time of the heating process for layer m, while $\tau_{\mathrm{m,cooling}}$ represents the counter-time required for the cooling stage. Specifically, λ is a constant

Table 3.2: Input value sets of the physical parameters

Name	Property [unit]	Value Set
Volumetric build rate	$\dot{V}\,[\mathrm{mm}^3/\mathrm{s}]$	$1,2,3,4$
Volumetric energy density	$VED\,[\mathrm{J}/\mathrm{mm}^3]$	$10,100,200,300$
Ratio of cooling duration	λ	$0,0.16667,0.5,1$
Biot number	Bi	$3.73134e^{-5}, 7.46269e^{-5}, 1.49254e^{-4}$

Table 3.3: Thermodynamic properties of Ti-6Al-4V lattice material

Name	Property [unit]	Value
Thermal conductivity	$k\,[\mathrm{W}/\mathrm{mm}\cdot\mathrm{K}]$	0.0067
Thermal diffusivity	$\alpha\,[\mathrm{mm}^2/\mathrm{s}]$	3.10497
Melting temperature	$T_m\,[\mathrm{K}]$	1900

ratio for all the printed layers. Then SLM process with no cooling stage and including the cooling time with the ratio λ of $1/6$, $1/2$, and 1 are selected to qualify their efforts on the thermal evolution for lattice materials. Recall that the Biot number (Bi) is used for describing the heat convection behavior during the cooling stage by the expression $Bi = h_c l_0/k$. The natural convective heat transfer coefficient for air ranges $5-25\ \mathrm{W/m^2\cdot K}$, thus the Biot number of $3.73134e^{-5}$, $7.46269e^{-5}$ and $1.49254e^{-4}$ are chosen as the input values of variable Bi.

In addition to the process parameters mentioned above, other significant physical parameter also evaluated in this paper is the width w. It defines the width of the square cross section of lattice struts. Generally, the lattice structures are composited of struts with a typical width from 0.3 mm to 1 mm, and struts in our lattice model has varying width within this range are applied for the evaluation. Eventually, the sets of these physical parameters are summarized in Table 3.2.

NUMERICAL PARAMETERS

In the previous stage, some physical parameters are addressed to study their influences on the thermal evolution of SLM-processed lattices. In other words, they are the inputted variables for our thermal model. By contrast, the numerical parameters, such as material properties and grid dimensions, are also the demanding inputs but have fixed values.

Ti-6Al-4V is the only metallic material we focus on in this study. For all the Ti-6Al-4V lattice structures, the concerning material properties for developing their thermal model including thermal conductivity k, thermal diffusivity α and the melting point T_m. It is easy to find that these material properties are temperature-dependent, and they are utilized to calculate the dimensionless parameters for Front-fixed approach introduced earlier. Specifically, it is assumed that these thermodynamic properties are constant and temperature-independent in our case for model simplification. The values used for various thermodynamic properties of Ti-6Al-4V are given in Table 3.3.

4

Results and Discussion

THE aim of this work is designing a numerical thermal process model to quantify the effects of various process parameters in combination with the choice of lattice geometry, on the development of the temperature field for SLM process. The results presented in this chapter can offer an insight on predicting the temperature field of lattices of interest, which is the pillar for predicting the SLM-processed part quality.

Modelling the thermal process of lattices during SLM is mainly divided into two stages, the heating stage and the cooling stage. Figure 4.1(a) uses a flow chart describing the overall thermal modelling process, while Figure 4.1(b) is the flow chart specified to both the heating stage and the cooling stage.

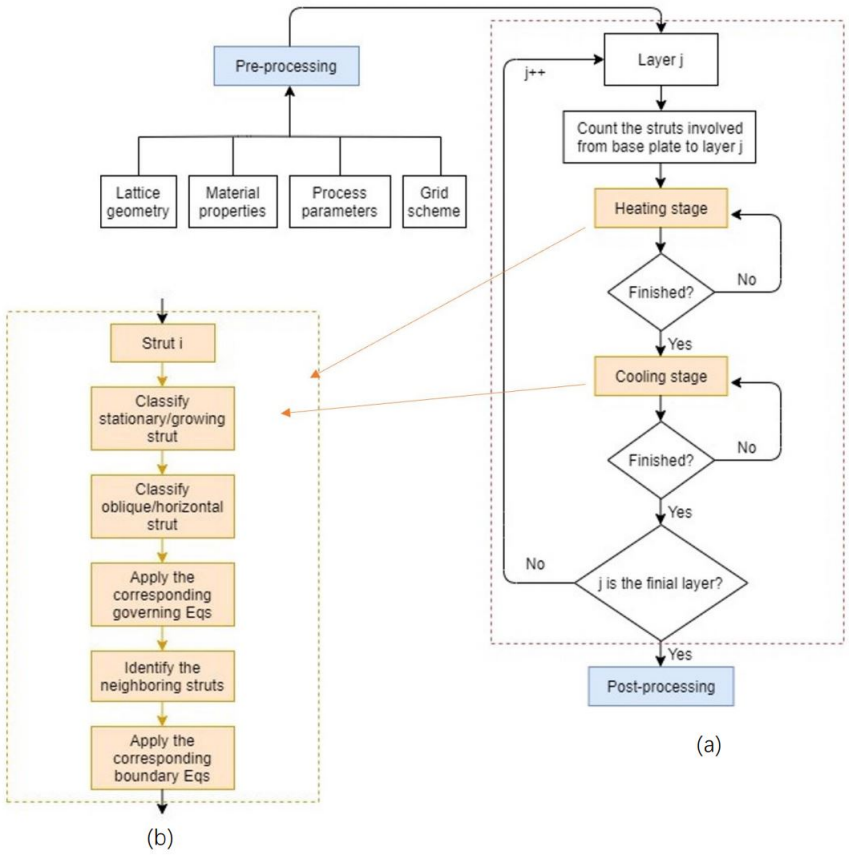

Figure 4.1: Flow charts to explain the numerical modelling of the thermal process of lattice developed by SLM. (a) gives the overall process for the thermal modelling. (b) is the flow chart focusing on the specified processes of both the heating stage and the cooling stage.

4.1. TRANSIENT TEMPERATURE FIELD OF LATTICES MANUFACTURED BY SLM

BY using the developed 2D thermal model based on the flow chart given in Figure 4.1, the temperature evolution of lattice components during cyclic heating and cooling processes of SLM are simulated. Meanwhile, during the simulation, a fixed set of process parameters is considered as listed in Table 4.1.

In this work, the thermal process for a single lattice strut can be addressed in normalized local coordinate ξ or X as a 1D model while expands to a 2D model for a lattice structure. Now consider the temperature field for a lattice structure, which consisting of a large number of struts. The

Table 4.1: Input parameters for modelling the thermal process of sampled hexagonal, square, and triangular lattice structures.

Name	Property [unit]	Value
Volumetric build rate	$\dot{V}$[mm^3/s]	4
Volumetric energy density	VED[J/mm^3]	10
Ratio of cooling duration	λ	1
Biot number	Bi	1.49254×10^{-4}
Width of strut	w[mm]	0.5

dimensionless coordinate ξ is defined according to the inclination of the oblique strut while the coordinate X is for the horizontal strut. In this regard, for oblique struts with different orientations, their local coordinate ξ refer to different directions. Based on the input parameters listed in Table 5.1, Figure 4.2 gives the temperature plots of a representative square lattice structure, which demonstrate the lattice temperature distribution when depositing a new layer during the SLM process.

For a simulated square lattice structure with dimensions of 16 mm×12 mm, there are 240 layers involved for a fixed layer thickness of 50 μm. It is evident that each metallic powder layer in a building lattice material experienced a similar thermal cycle: heating, cooling, reheating, and re-cooling. To be more specific, Figure 4.2(a) describes the temperature distribution for a square lattice structure when the layer 239 is melted during the heating stage, which is so-called state 1. After that, a cooling stage is following, and Figure 4.2(b) display the temperature profile of a square lattice at the end of cooling stage and it is so-called state 2. Once consolidating the layer 239, a new layer 240 is introduced to repeat such heating-cooling process and Figure 4.2(e) and Figure 4.2(f) depict the lattice temperature distribution for the heating (i.e., state 3) and cooling stage (i.e., state 4), respectively. Meanwhile, the layers below layer 240, such as layer 239, are re-melted and re-solidified. In a SLM process, such heating-cooling cycle is repeated until the whole lattice structure is completed.

It is worth noting that the curves in Figure 4.2(c), Figure 4.2(d), Figure 4.2(g), and Figure 4.2(h), indicate the change of the average temperature and the maximum temperature during the two heating-cooling cycles. Obviously, the maximum temperature of the modelled lattice structure elevated once it is experiencing the heating process whilst decreased during the cooling stage as depicted in Figure 4.2(d) and Figure 4.2(h). Consider now the average temperature plots. For the first two states, the work cycle of layer 239, The interesting thing is, such average temperature plot has an increased trend for the deposition of layer 239 as given in Figure 4.2(c), on the contrary, it is decreased during the second heating-cooling cycle as shown in Figure 4.2(g). As mentioned before, our thermal model takes both the thermal conduction and thermal convection into account. In this regard, the raising average temperature after the cooling stage for the layer 239 can be explained as the concentrated heat on the building layer flowing to the layers below it by heat conduction. Meanwhile, this phenomenon also indicates the convection consuming a relatively small proportion of the total heat transfer and the conduction significantly dominating the heat dissipation whilst the layer 239 being constructed by SLM. Besides, the primary distinction between the layer 239 and the layer 240 is the layer 240 consisting of four horizontal struts. Recall that the heat dissipation due to thermal convection is occurs on the top boundary surface of our lattice model, i.e., on the building powder layer. It can be considered that the surface area of the constructed struts experiencing the heat convection is much larger for the later case. Therefore, a better cooling performance is reasonably investigated for the fabrication of the layer 240.

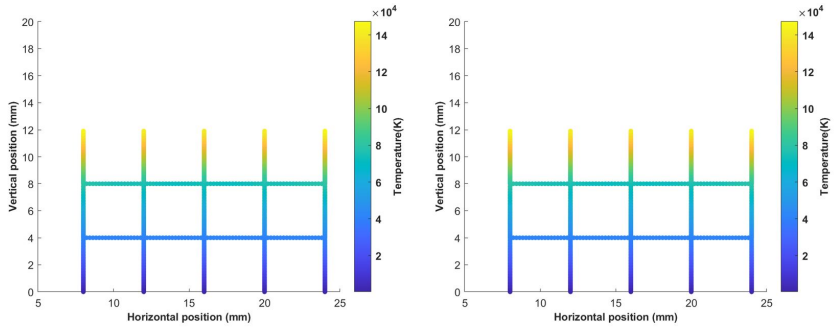

(a) State 1 (b) State 2

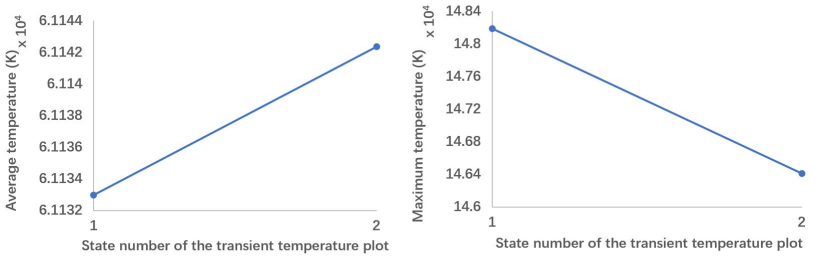

(c) Average temperature plot for state 1&2 (d) Maximum temperature plot for state 1&2

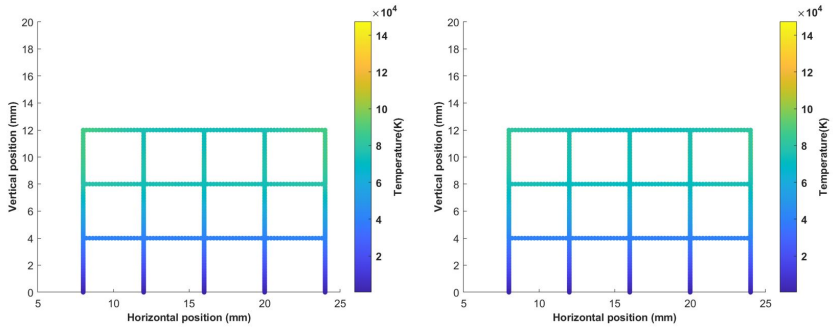

(e) State 3 (f) State 4

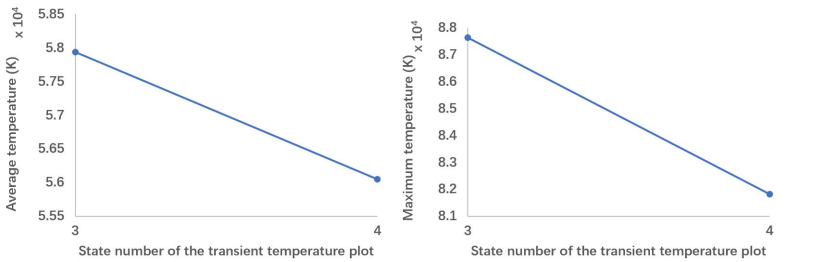

(g) Average temperature plot for state 3&4 (h) Maximum temperature plot for state 3&4

Figure 4.2: Two complete heating-cooling work cycles in SLM process for a sampled square lattice when a new layer of powder is deposited. (a) represents contour plot when the layer 239 is melting (i.e., state 1) while (b) is after the cooling stage (i.e. state 2). (c) and (d) are the average temperature plot and the maximum temperature plot from (a) state 1 to (b) state 2, respectively. Similarly, (e) gives the temperature distribution after the heating process of a new layer 240 (i.e., state 3) while (f) is for the end of the cooling process (i.e., state 4). Meanwhile, (g) and (h) are the average temperature plot and the maximum temperature plot from (e) state 3 to (f) state 4, respectively.

However, it can be easily found that the computed temperature fields display an extremely high value relative to the melting point of the chosen material Ti-6Al-4V, which is around 1900 K. It can be considered that the selected ranges of varying process parameters are all for fabricating a real lattice structure in 3D case. Herein, our 2D lattice model is regarded as having a thickness of a unit strut width in the excluded third direction. That is to say, the modeled lattice structure is probably much smaller than a typical lattice material in a practical case and therefore the chosen process parameters are not suitable. Another important factor might cause this problem is the simplification of the heat transfer behavior. Specifically, not only the thermal radiation, but also the heat conduction between metallic particles and consolidated lattice struts are ignored in our thermal model. They are both attributing to the heat dissipation, especially for the latter, play an important role for the heat loss of a lattice porous structure. Consequently, the lack of the consideration of these two heat transfer behaviors potentially leads to the excessive temperature results. Although the proposed thermal model is unable to provide the temperature result with a reasonable value, it is still effective for analyzing the general variation trend of the temperature field with respect to process parameters and lattice architecture.

4.2. EFFECT OF THE COOLING PARAMETER λ

RECALL that the cooling parameter λ representing the ratio of the cooling duration to the heating duration for a single heating/cooling cycle during the SLM process. λ=1 means the cooling duration is equal to the heating duration in the same heating/cooling cycle. In general, the heating stage extends a longer period than the cooling stage in a typical SLM process. Herein the λ takes three different values, 1/6, 1/2, and 1, to investigate its influence on the thermal evolution of a lattice during SLM. Based on the developed thermal model, a lattice structure constructing with repeated square unit cells is simulated with varying λ values. Besides, the other parameters applied for the simulation are listed in Table 5.1. Figure 4.3 gives four curves of the temperature fields along the top four horizontal struts of a square lattice in different cooling conditions.

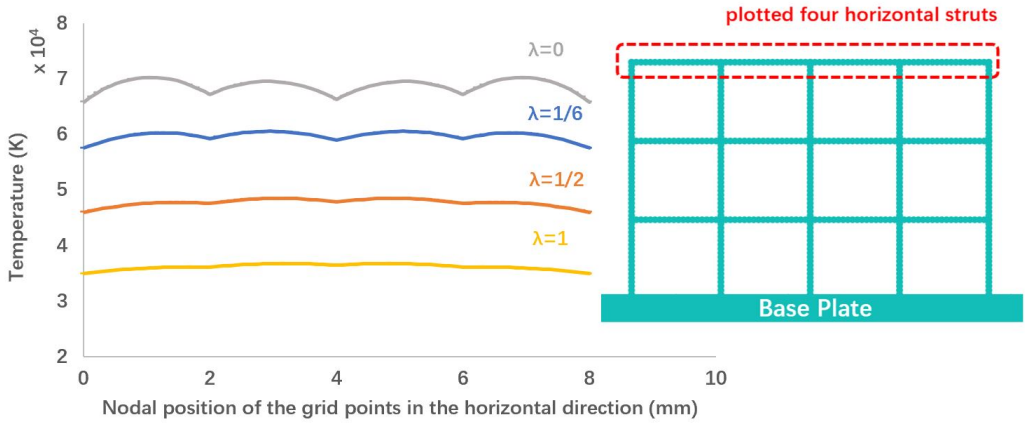

Figure 4.3: Temperature distribution along the horizontal struts on the top surface for a square lattice structure. The analysed layer is highlighted by a red dotted box given in the figure on the right-hand-side. Different trend lines indicating the simulated results with varying cooling parameters λ ranging from 0 to 1. Herein all the other process parameters are chosen as the values given in Table 5.1 except for the $\dot{V}$, which is defined as 1 in this case.

In general, during the heating process, the temperature field along a single building horizontal strut has a peak near its central position, and the lowest temperature is always located on the two

sides where the vertical strut is connected. This phenomenon is clearly expressed by the gray line in Figure 4.3, which represents the case when no cooling stage being taken into account. Consider now including the cooling stage by the cooling parameter λ. It is obvious that the temperature trend lines, as shown in Figure 4.3, become flatter for a longer cooling duration. Such result reasonably explains that the cooling process is beneficial to reduce the thermal gradients along struts. As stated in the early stage, large temperature gradients resulting in high levels of residual stress within the additively manufactured lattice structures, so part distortion may occur. Hence, analyzing the influence of the cooling duration can provide a basic insight into the lattice quality improvement.

In sum, a higher cooling parameter λ implies a lower average temperature and a lower level of the temperature gradient for a building lattice material.

4.3. EFFECT OF THE LATTICE ARCHITECTURE

FOR a lattice structure, it is well-known that its architecture can be a major factor altering its temperature distribution. Specifically, the architecture of a lattice structure can mainly be attributed to the four aspects: the elementary cell configuration, the unit cell size, the unit cell orientation, and the total number of connectivity of a lattice (N_c). Note that the total connectivity N_c of a lattice is calculated by adding the connectivity of all the nodes. For example, consider a square lattice as given in Figure 4.4 and nodes with different connectivity are indicated by different colors, its N_c is determined as $N_c = 5 \times 1 + 7 \times 3 + 2 \times 2 + 6 \times 4 = 54$.

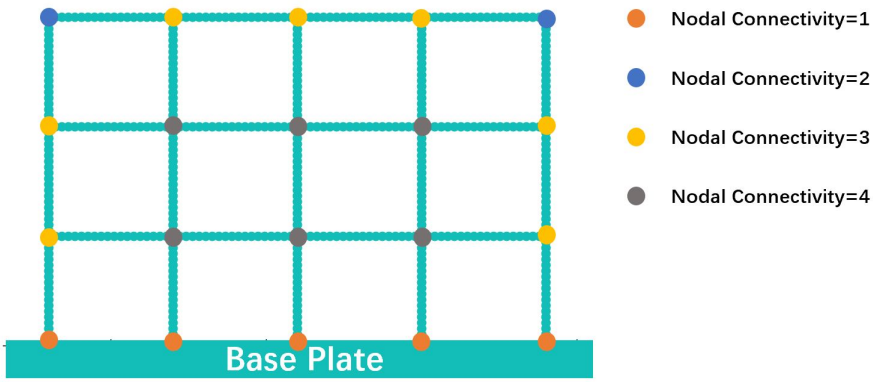

Figure 4.4: Schematically description of the nodal connectivity for a representative square lattice structure. Herein nodes with varying connectivity are highlighted by different colors, which are labelled on the right-hand-side.

Starting from the first factor, the unit cell configuration. Three types of lattice structures are investigated in this work, the Triangular (T) lattice, the Square(S) lattice, and the Hexagonal (H) lattice. Accordingly, Figure 4.5 lists the periodic unit cells for the representative lattices, where the red dash lines drawing the shape of the unit cell and black lines indicating the lattice members included in a single unit cell. For a better comparison, all the lattice structures are designed to have a size 16 mm ×12 mm as displayed in aforementioned Figure 3.1(b). Besides, it is assumed that a single unit cell containing equilateral lattice members. For instance, in a square unit cell given in 4.5, the lattice members indicated by black lines are having the same length L_S. When all the unit cells are designed with the same width, namely W_H=W_T=W_S as shown in Figure 4.3, the relation among L_H, L_S and L_T can be derived as,

$$L_S = L_T = 2L_H = W, \tag{4.1}$$

In this work, W takes a value of 4 mm, which is a typical unit cell width for a metallic lattice structure. Therefore, the strut lengths of the three unit cells can be calculated as following equations and the dimensions of unit cells are indicated in Figure 4.5.

$$L_S = 4\text{mm}, \tag{4.2}$$

$$L_T = 4\text{mm}, \tag{4.3}$$

$$L_H = 2\text{mm}, \tag{4.4}$$

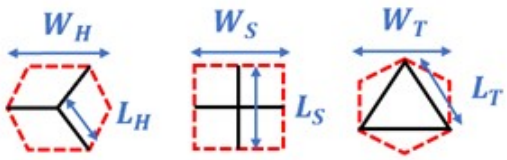

Figure 4.5: Schematic illustration of the dimensions for varying types of unit cell. Specifically, the red dash lines draw the shape of the unit cells and the black lines are for the included struts inside the defined unit cells.

Based on an identical cross-sectional width of struts, 0.5 mm, Figure 4.6 (a) to (c) display the temperature field profiles of the three lattices. Furthermore, Figure 4.7 plots the average temperature results for these lattices when varying heating-cooling ratio λ is applied. Note that the process-related productivity $\dot{V}$ is selected as 1 mm^3/s for the simulation work.

As indicated in Figure 4.7, the triangular lattice has the lowest average temperatures while the hexagonal lattice is highest. For instance, when the cooling ratio λ=1, the average temperature for the triangular lattice is $T_{\text{avg,T}}$=2.17 × 10^4 K. while the hexagonal lattice has the largest $T_{\text{avg,H}}$=2.60 × 10^4 K. Besides, the average temperature of the square lattice has an intermediate value among them, which is $T_{\text{avg,S}}$=2.45 × 10^4 K. For different unit cell configuration, the paramount distinction is their nodal connectivity. Recall that the connectivity for the three lattices of interest in Figure 4.6 (a) to (c) are 6, 4, and 3, respectively. For a lattice material with a higher connectivity, which implies that a higher number of members are connected in the same node. That is to say, during SLM heating process, such lattice structure will have a better ability for the global thermal conduction through the intersecting nodes. Hence, among all the three sampled lattice structures, the triangular lattice is found to provide the best heat transfer efficiency, whereas the hexagonal one is the least efficient.

Besides, another crucial factor affecting the thermal performance of the SLM-processed lattice structure is the size of the unit cell. Consider now a representative square lattice with a series of cellular sizes ranging from 0.5 mm to 8 mm, and Figure 4.8 indicates the relationship between the elementary cell size and the simulated average temperature.

As indicated in Figure 4.8, there is a corresponding temperature profile for every data point. It is thus worth noting that a lattice will involve more connection points if its repeated cell has a smaller size, which implies a better ability for the thermal conduction through the intersection nodes. Based on that, the square lattice consists of the smallest elementary cells, 0.5 mm×0.5 mm, presenting the lowest average temperature in Figure 4.8. Furthermore, the lattice average temperature is elevated when the size of the square cell is increased.

Eventually, the last two aspects, the unit cell orientation and the total connectivity of a lattice, are combined to discuss their effects on the temperature evolution for a SLM-processed lattice

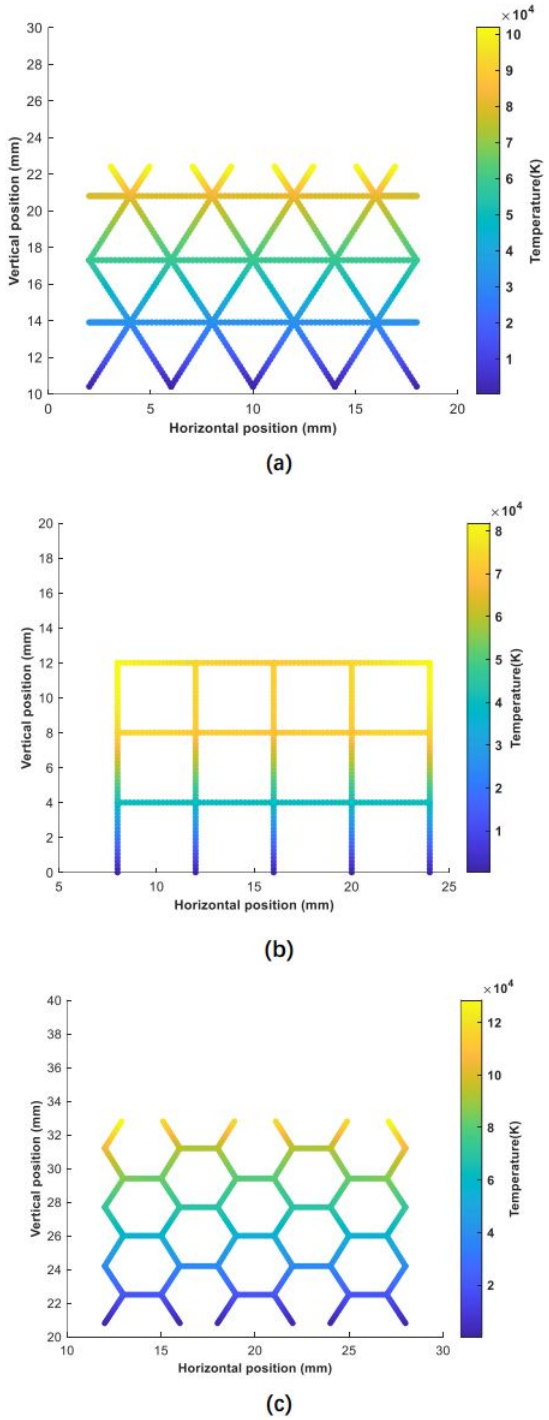

Figure 4.6: Temperature field profiles for lattices composited of varying unit cells. (a) is the temperature profile for a lattice structure consists of repeated triangular unit cells. (b) gives the temperature distribution for a lattice structure consists of repeated square unit cells. (c) is the temperature profile for a lattice structure consists of repeated square unit cells.

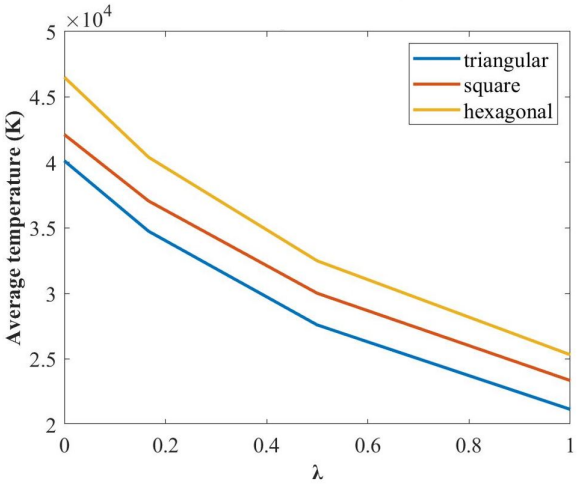

Figure 4.7: Sampled average temperature results after the end of the cooling stage of layer 240 (i.e., the SLM process is finished) for three basic types of lattices: hexagonal lattice structure, square lattice structure, and triangular lattice structure. Herein $\dot{V}$ equals to 1 mm^3/s and varying cooling parameter λ ranging from 0 to 1 are applied.

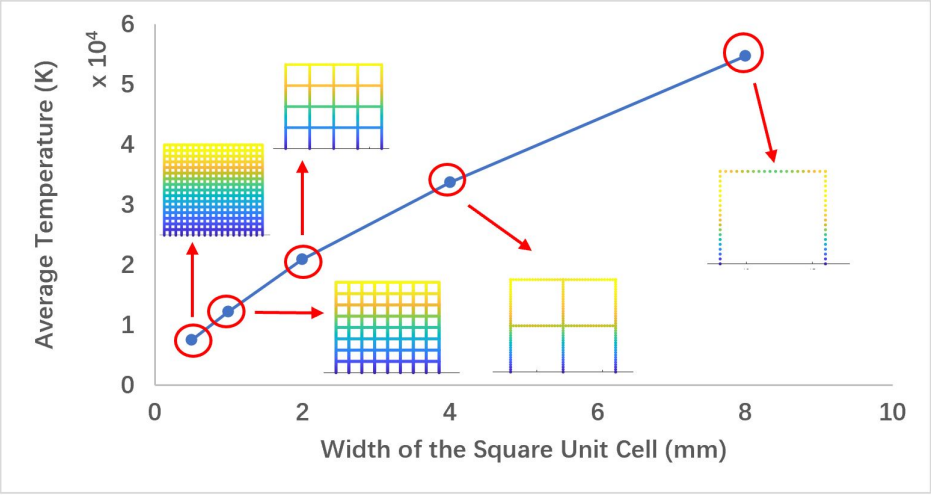

Figure 4.8: Average temperature plot for lattice structures constructed with varying sizes of square cells. The length of the square unit cell is changed from 0.5mm to 8mm for the simulation. Each lattice member is discretized to 21 grid points and thus the temperature plot for struts are shown as dotted lines.

structure. Herein the square unit cell is selected as the sampled unit cell type again. First, consider now the definition of unit cell orientation. In this study, three generic unit cells with the orientations given in Figure 4.5 are termed here as their initial status (i.e., rotation angle equals to 0 degree). In fact, the architecture of the resulted lattice might be changed if its unit cell is rotated but remaining a same shape. For a square unit cell, there are six rotation angles are involved for the analysis: 0°, 15°, 30°, 45°, 60°, and 75°. It is worth mentioning that the square unit cell will back to the initial status when it has an orientation of 90 degrees. Based on that, three sets of square lattice structures constructed with varying orientated unit cells are considered according to three chosen total number of connectivity N_c: 54, 60, and 64, which is defined previously as depicted in Figure 4.4. For all the sampled lattices, the overall cost of the metallic lattice materials is set as close to each other as possible by fixing the total length of all the lattice members for a more accurate comparison. Therefore, Figure 4.9 describes how the total number of connectivity (N_c) and lattice orientation comprehensively affects the temperature performance of a lattice structure.

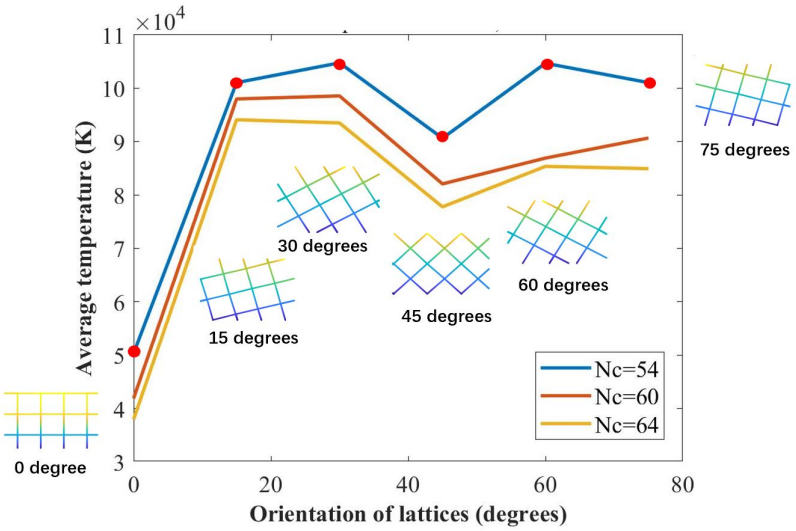

Figure 4.9: Average temperature plot for lattice structures constructed with varying cell arrangement to achieve different overall nubmers of connectivity N_c. There are six orientations are evaluated for all the lattice types: 0°, 15°, 30°, 45°, 60°, and 75°. The temperature plots of lattice with these six orientations are also given in this figure. Specifically, the entire contour plots are detailed in Appendix A. Herein $\dot{V}$ equals to 4 mm^3/s and cooling parameter λ 1 is applied.

The three curves shown in Figure 4.9 are corresponding with the three representative connectivity numbers N_c. On the basis of a fixed unit cell orientation, the analysis (Figure 4.9) indicates that a lattice with a lower connectivity has an elevated level of the average temperature result. Varying N_c numbers refer to differ unit cell arrangements when constructing a square lattice structure. In fact, the higher connectivity implies a better thermal conduction ability. Thus, for the three chosen lattice total number of connectivity, lattices with N_c number equals to 64 are found to enable the best heat transfer efficiency, whereas the lowest connectivity cases (i.e., N_c=54) provide the least efficient.

In addition, it is obvious that the plots for both the cases N_c=60 and N_c=64 have a similar general trend as the average temperature plot when N_c=54. Generally, the unit cell orientation has a certain impact on the thermal evolution of a lattice structure. However, the simulated results given in Figure 4.9 are insufficient for identifying such impact concretely. It merely states that the cases with orientated angle 45° always perform a better heat transfer efficiency if without the consideration of the square lattices in the initial status. To clearly investigate the mechanism of how the lattice orientation influences the average temperature result, the average orientations of lattice

members for all the representative lattice structures included in the case of N_c=54 are determined and are listed in Table 4.2.

Through dividing the sum of the strut orientations by the total number of the struts, the average orientation of the lattice members can be calculated. The specific calculation steps are presented in Appendix A. Based on the data listed in Table 4.2, it can be found that for a square lattice structure with higher rotation angle, the average orientation of its members becomes larger. However, such increased trend is not in coincidence with the fluctuated plots given in Figure 4.9. Unfortunately, this work is failed to offer a reliable statement about the effects of the average strut orientation on the temperature result.

However, there is an interesting investigation associated with the effect of the horizontal struts on the thermal evolution of a lattice. As exhibited in Figure 4.9, the average temperature results for lattices with different rotations are fluctuated in a certain range except for the initial status. The primary distinction between the initial status and other status are the existence of the horizontal struts. The average temperature results shown in Figure 4.9 illustrate that the horizontal strut can have positive impact on the lattice heat transfer and heat dissipation. To further verify this statement, the triangular lattice structures and the hexagonal structures are simulated. Table 4.2 lists the representative elementary cells of triangular and hexagonal lattices for both the initial status and the status of rotating 30 degrees. Similarly, lattices in their initial status involve at least one horizontal strut while zero for the orientated cases sampled in Table 4.2. Compared to the thermal results of these two lattices in their initial status with the horizontal struts, lattices excluding these horizontal struts exhibit a relatively lower level of average temperature as presented in Figure 4.10.

Accordingly, the above simulation results tend to indicate that the existence of the horizontal strut has the potential for impairing the heat transfer behavior of the proposed lattice geometries in this section.

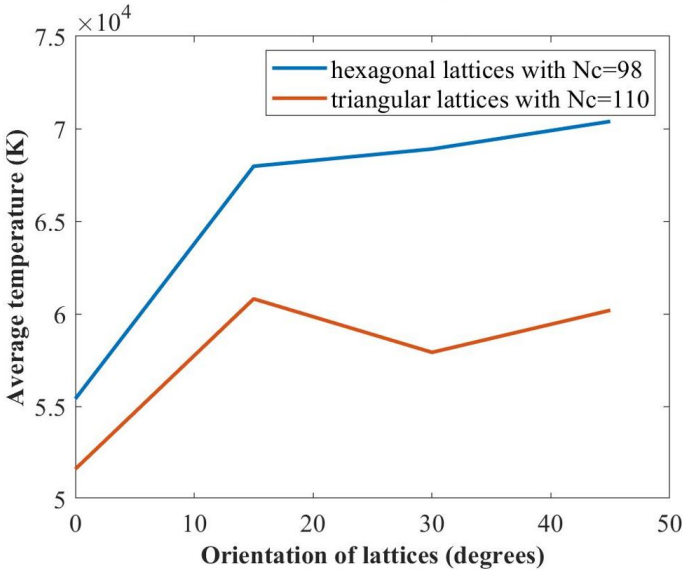

Figure 4.10: The average temperature plots for lattices with a constant N_c number and different orientations after finishing the SLM process. Note that the horizontal struts only exsit for the orientation equals to 0°. Two types of the lattice structures are considered: triangular lattices and hexagonal lattices. Herein $\dot{V}$ equals to 4 mm^3/s and cooling parameter λ 1 is applied.

Matching the conclusion stated before, the results shown in Figure 4.10 demonstrates that the

Table 4.2: Average orientations of struts and the temperature distribution plots of square lattices with varying rotation angles. Herein a constant total connectivity (i.e., N_c=54) is considered for all the listed cases.

Lattice rotation angle	2D geometric description	Average orientation of members
0°	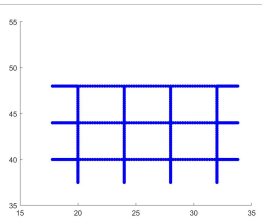	42°
15°	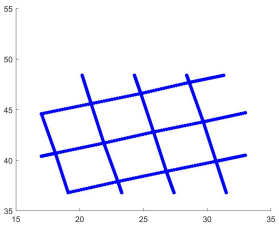	59.1746°
30°	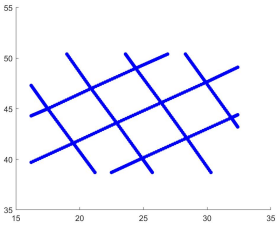	76.4004°
45°	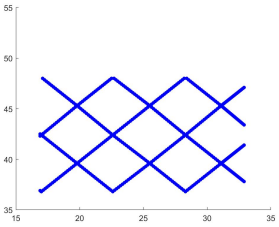	89.9992°
60°	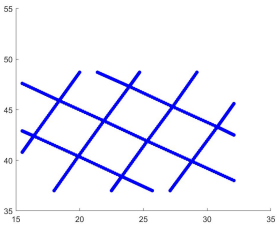	103.6508°
75°	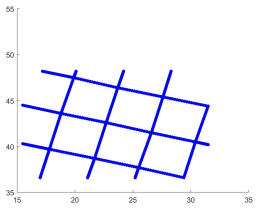	120.8254°

existence of the horizontal struts might lead to lower temperature result for not only the square lattices, but also the hexagonal lattice structures and triangular lattice structures. During the cooling stage of a SLM process, it can be considered that the thermal convection in a horizontal strut is enhanced due to its larger surface for the heat dissipation.

In sum, evaluating the contributions of the above four aspects associated with the lattice topology could be assisted in the transient temperature prediction for a known lattice architecture.

4.4. EFFECT OF THE VOLUMETRIC BUILD-UP RATE $\dot{V}$

The printing speed is a crucial process parameter that affects the heat transfer of a lattice structure whilst it being built by SLM. In the designed thermal model, a dimensionless growth rate $\dot{H}$ is defined for the simulating the lattice temperature evolution. Recall that $\dot{H}$ value is calculated by $\dot{H} = \frac{\dot{l} l_0}{\alpha}$, and the term printing speed $\dot{l}$ strongly depends on the total cross-sectional area of the members in the currently building layer. In other words, the value of $\dot{H}$ might change for different processing powder layers. Although quantifying the effect of the parameter $\dot{H}$ enables a comprehensive evaluation of two factors: the printing speed and the thermal diffusivity, its unfixed value during the SLM process is a huge challenge. Alternatively, a constant process parameter, $\dot{V}$, is discussed in this study. The volumetric build up rate $\dot{V}$ defines the production rate for fabricating a lattice structure with a certain volume of material.

In this section, the process parameter $\dot{V}$ is evaluated for three lattices constructed by square unit cells, triangular unit cells, and hexagonal unit cells. Figure 4.11 (a) to (d) represent the modelled SLM-processed condition with the cooling ratio λ in a value of 0, 0.1667, 0.5, and 1, respectively. By comparing the average temperature results for the three representative lattice structures at different productivity $\dot{V}$ in the combination with different cooling ratio λ, it can be investigated how the build up rate affects the temperature evolution of various lattice structures.

As shown in Figure 4.11 (a) to (d), in all the four cases with varying cooling parameter λ, for higher build up rate scenarios, all the simulated lattice structures present an elevated average temperature result. In general, the process-related build-up rate is limited amongst other factors by the available heat input power. Recalling that the energy density VED defines the ratio of power to the build up rate $\dot{V}$, which remains to be 10 mm^3/s during the simulation work in this section. This implies that, using a higher power input, can achieve a higher process productivity. Consequently, such increasing trend depicted in Figure 4.11 is understandable as such high applied heat is harder to dissipate and cool down, especially for materials with low thermal conductivity like the selected metallic material Ti-6Al-4V in this work.

Moreover, although the general trend of the three curves are very similar for all the productivity cases, the average temperature growth rate of lattices with different elementary cell configurations still have different performance. As given in Figure 4.11 (a), the blue curve for the triangular lattice structure has a larger growth rate than the other two lattices. Specifically, this blue curve is initially (i.e., $\dot{V} = 1 mm^3/s$) lower than the red curve for the square lattice structure while above it at the end of the curve (i.e., $\dot{V} = 4 mm^3/s$). However, such higher growth rate is gradually diminished from Figure 4.11 (a) to (d), where the cooling ratio λ is increased from 0 to 1. Thus, it can be stated that the triangular lattice shows a better potential on elevating the average temperature when the build up rate is increased by the same amount, and this increment is enhanced for a lower cooling parameter λ. One possible explanation of this investigation is that, when there is no cooling stage taken into account (i.e., $\lambda = 0$), the larger heat input in a high build up rate $\dot{V}$ such as 4 mm^3/s

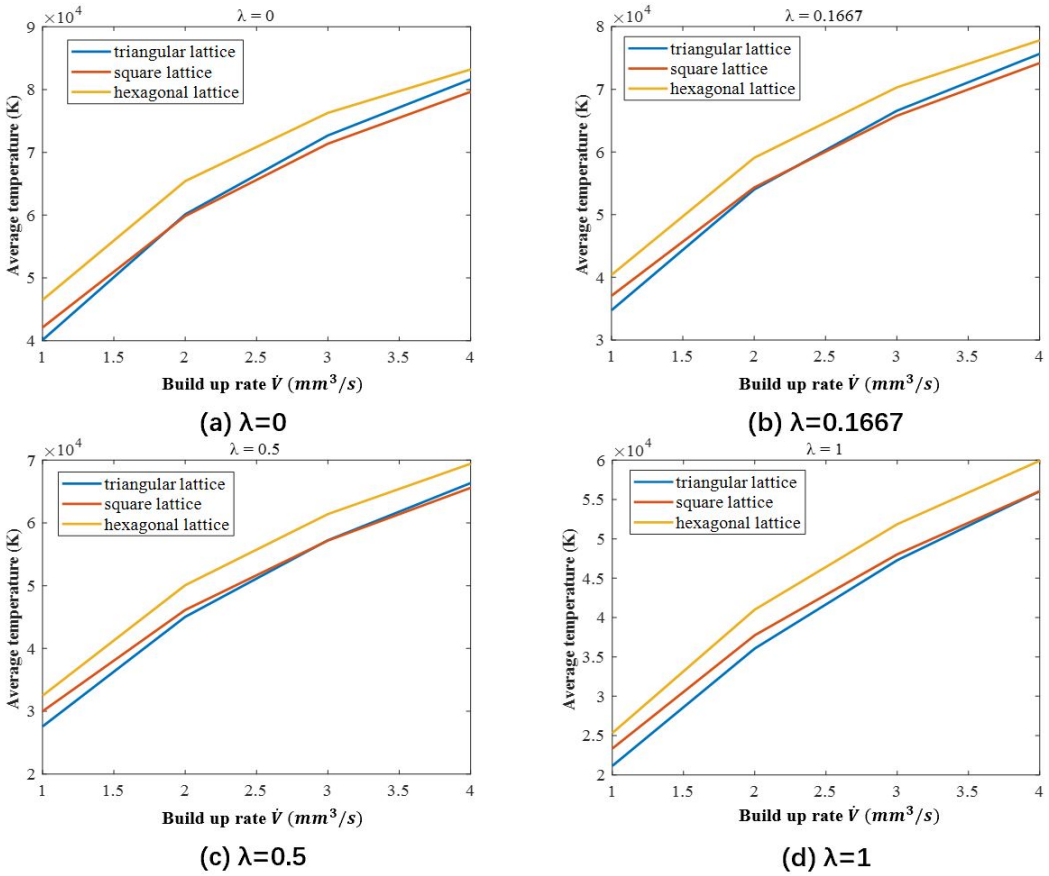

Figure 4.11: Sampled average temperature plot for a square lattice structure under varied volumetric build up rate ranges from 1 mm^3/s to 4 mm^3/s. (a) to (d) represent the process conditions with four different cooling ratios λ equal to 0, 0.1667, 0.5, and 1, respectively. Other process parameters, VED, $\dot{V}$, and Bi values are set to be 10 J/mm^3, 1, and 1.49254×10^{-4}.

might imply a better heat transfer for a triangular lattice due to its higher nodal connectivity. In contrast, when a certain cooling ratio is applied, the heat dissipation by heat conduction also more efficient in the triangular lattice case.

4.5. EFFECT OF THE ENERGY DENSITY VED

As defined in the early stage, the energy density is one of the SLM process parameters formulating as $VED = \frac{power}{\dot{V}}$. Evaluating the energy density enables an insight into how the heat input power and the productivity comprehensive affect the thermal flow within SLM lattice structures. In this section, different combinations of process parameters with varying energy density levels are utilized to simulate the proposed lattices, where the value of VED has a typical range from 10 J/mm^3 to 300 J/mm^3. Herein the values of other process parameters are all taken from Table 4.1. Accordingly, the curve given in Figure 4.12 presents the relationship between the defined energy density and the resulted average temperature of the sampled square lattice model.

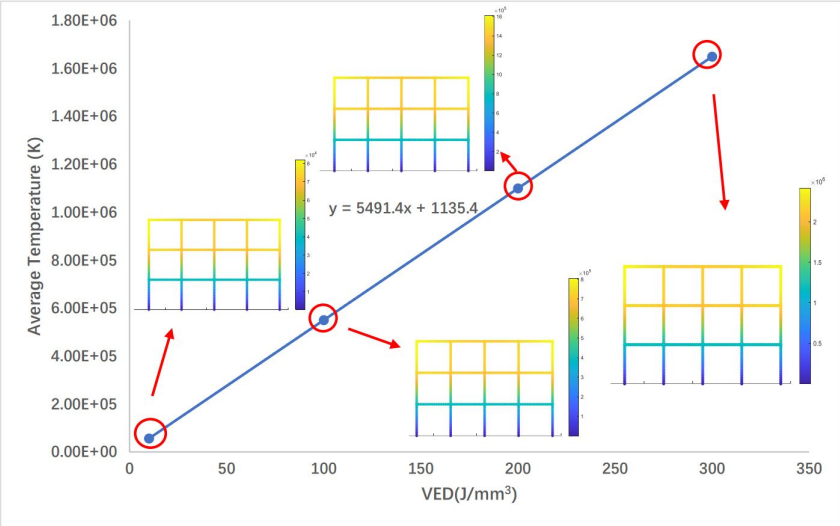

Figure 4.12: Sampled average temperature for a square lattice structure when applying different energy density from 10 J/mm^3 to 300 J/mm^3.

In a real SLM process, a low energy density can result in insufficient melting so that limited densification of the fabricated lattice materials. However, applying an extremely high energy value might lead to fully melted particles resulting into lower porosity of components and thus a high hardness value [70]. Although the values of resulted average temperature given in Figure 4.12 are all much higher than the melting point T_m=1900K and a proper energy density is hard to be identified, the linear relationship between the energy density VED and the average temperature is still investigated. Specifically, such linear variation has a slope equal to 5491.4 as shown in figure 4.12.

4.6. EFFECT OF THE BIOT NUMBER Bi

In the aforementioned section, the Biot number is proposed as a key factor in integrated connecting the thermal conductivity k and convection coefficient h_c for the cooling stage of SLM process. Consider now three different values of Biot number listed in Table 3.2. Similar with the previous section, other process parameters are chosen as the values given in Table 4.1. To examine the influence of the Biot number on the development of the temperature field, the thermal evolution of the proposed square lattice structure is simulated, and the results are displayed in Figure 4.12

below.

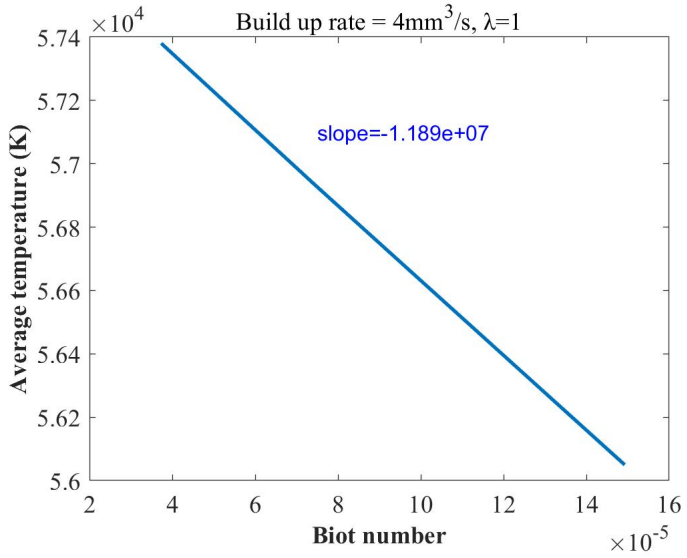

Figure 4.13: Sampled average temperature curve for three different values of the Biot number, 3.73134×10^{-5}, 7.46269×10^{-5}, 1.49254×10^{-4}. Other applied process parameters are given in Table 5.1.

A larger Biot number can both imply that the component has a worse thermal conduction ability or performs better on dissipating heat by natural convection. The heat loss during the SLM process is mainly attributed to the heat conduction as the values of the Biot number typically in a very low level with the order of 10^{-4} or 10^{-5}. Therefore, it is reasonable that an increased Biot number leads to a lower average temperature result due to the higher overall cooling efficiency. This statement is perfectly verified by the simulation results shown in Figure 4.13. In addition, it also proves that the Biot number is negatively and linearly correlated to the average temperature result of the sampled lattice structure.

4.7. COMPUTATIONAL COST AND CONVERGENCE STUDY

Recall that the maximum time step size $\Delta\tau$ requiring for the stability condition is determined in the early section 4.2.4, either $\Delta\tau \leq \frac{H^2\Delta\xi^2}{2}$ for oblique struts or $\Delta\tau \leq \frac{\delta X^2}{2\beta^2}$ for horizontal struts. Particularly, combining the known values of the associated parameters H, $\Delta\xi$, $\Delta\tau$, ΔX, and β with the derived stability equations, it can be found that the maximum dimensionless time step enabling the stable thermal results for a designed lattice structure is $\Delta\tau \leq 1.3850 \times 10^{-3}$.

However, stable results are insufficient to support any reliable investigation in this study. With this purpose, convergence analysis in Figure 4.14 is performed by decreasing the size of normalized time step $\Delta\tau$ from 0.001 to 0.000005. Meanwhile, the total number of time steps in demand becomes higher due to the constant normalized time parameter τ during the simulation.

The convergence plot shown in Figure 4.14 exhibits that the converging behavior starting from the point B, where the time step has a size of 0.0001 and the corresponding number of time step is $n\tau = 3.75 \times 10^7$. That is to say, the maximum time interval $\Delta\tau$ is 0.0001 for obtaining a reliable temperature result. Consider now the computational cost for applying different sizes of the time step $\Delta\tau$. As stated in the early stage, improving the computational efficiency will be challenging when a SLM-processed lattice material is modeled. In this regard, balancing the result accuracy and the computational cost, is another key point discussed in this section.

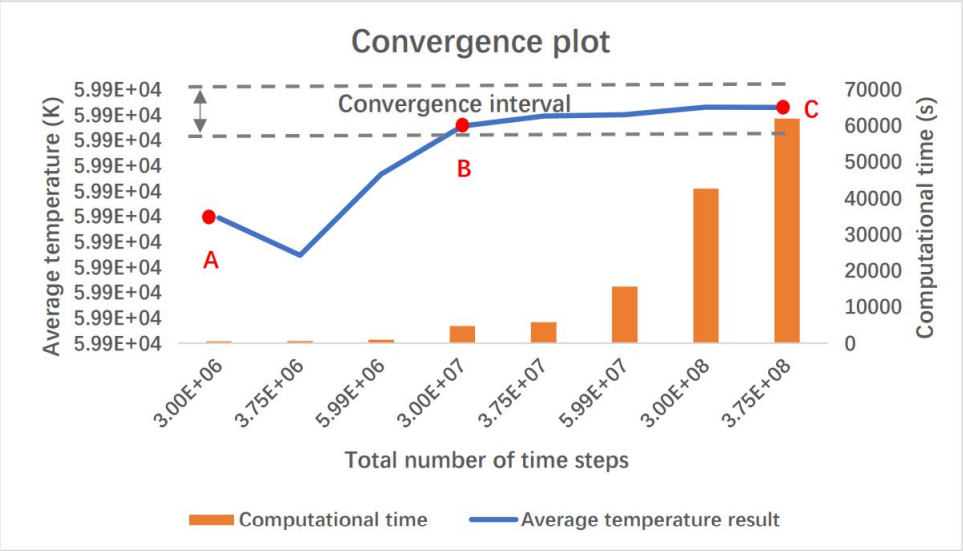

Figure 4.14: Convergence plot when using different number of time steps for the temperature evolution calculation. Point A is for each time step equals to 0.001s; Point B is for each time step has a size of 0.0001s and this is the convergence point for our modelling work; Point C is for a time step equals to 0.00005.

Noteworthy in Figure 4.14, the height of the given bars represents the cost of overall computational time for simulating the thermal evolution of a square lattice structure whilst it being built by SLM. Obviously, the amount of the simulation time will be dramatically increased when the size of the time step is further reduced. To be more specific, the thermal evolution simulation in Point C (i.e., $\Delta\tau$=0.000008) displays a computational time approximately 128 times of the case in Point A (i.e., $\Delta\tau$=0.001). In contrast, consider now the determined convergence Point B (i.e., $\Delta\tau$=0.0001), Figure 4.14 indicates a 90.64% reduction on the computational cost compared to the result on Point C. Although a larger number of time steps represents a more precise calculation, using a proper time step is primary due to the consideration of the simulation efficiency. Accordingly, the simulation time step is selected to be 0.0001 in this work.

This convergence study aims to investigate a proper size of the normalized time step $\Delta\tau$ based on the comprehensive consideration of both the computational cost and the result accuracy. Therefore, all the results presented in this work are simulated in accordance with the chosen value of $\Delta\tau$, 0.0001.

5

Conclusion and Recommendations

In this study, a moving grid method is proposed and therefore a thermal model is developed for a designed lattice structure whilst it being built by SLM process. Through applying this model, the temperature evolution of differ lattice structures in combination with varying process parameters are simulated to understand their effects. The simulation results of this study will facilitate the enhancement of the products quality of the SLM manufacturing technique for a metallic lattice structure. In this chapter, the key findings based on the present work are summarized, and recommendations for further research directions are given.

5.1. CONCLUSION

This paper aims to have a better understanding of the evolution of the temperature field during the fabrication of lattice materials through numerical simulation. For this purpose, we have addressed modelling of lattice structures during the SLM process, basing on the moving grid method and the Front-tracking Finite Difference approach, and evaluated the influences of lattice topology and different process parameters on the thermal history. Eventually, in accordance with the simulation results, the following conclusions can be drawn:

- The topology of a lattice structure plays a crucial role in deciding the transient temperature field of a lattice structure. Specifically, among the three selected lattices with different unit cell configurations, the triangular lattice is found to offer the best heat transfer efficiency while the hexagonal lattice has the lowest heat transfer efficiency. Besides, the average temperature is elevated with larger size of the unit cell. Furthermore, summing up the total connectivity of all the struts of a lattice structure can assist in predicting the level of its average temperature, where higher connectivity implies a lower temperature result. Moreover, the existence of horizontal struts tends to impair the heat transfer behavior of the lattice of interest.
- Higher build up rate $\dot{V}$ can lead to an increased average temperature of a SLM-processed lattice structure. Such enhancement is more pronounced in the triangular lattice and is diminished for a longer cooling duration in SLM process.
- Higher applied energy density VED can linearly elevate the temperature field of a lattice
- Higher Biot number Bi, which quantifies the thermal conductivity and the ability of heat convection comprehensively, can cause a decrease in temperature field of a lattice structure.

Note that a proper dimensionless time step $\Delta\tau$=0.0001 was determined through a convergence analysis, which is an excellent choice to consider the result accuracy and the modelling efficiency comprehensively. Based on that, all the mentioned results above are simulated in accordance with this selected time step.

5.2. FUTURE WORK

In this thesis, the proposed growing grid model for a SLM-processed lattice under several prescribed assumptions and simplifications. For the purpose of improving this work, future research direction can be concluded mainly in the following aspects:

- Thermodynamic material properties, such as thermal conductivity k and the heat coefficient h_c, are the temperature-dependent properties. Thus, these thermal properties should be accurately defined based on the local instantaneous temperature value of the simulated lattice.
- In this work, a linear growth rate is considered, and the lattice members are discretized by equidistant grid points. For a real SLM manufacturing process, the building lattice members

might have a nonlinear growth rate of its length. A possible approach to solve the nonlinear growth rate is using unevenly spaced grid points with different sizes for the discretization.

- The moving grid method is the only modelling approach involved in this work. It is possible that take other methods, for example, the traditional FEM, into account for the comparison. Based on that, the benefits of applying the moving grid method can be identified, and the accuracy of the moving grid method can be further verified.
- The proposed thermal model is for a lattice structure in 2D domain. To make the model more realistic, it is suggested to expand the thermal model into 3D domain. In this case, the problem of the extremely high temperature field in our simulated results might be solved.

REFERENCES

[1] M.Kniepkamp, J.Harbig, C.Seyfert, E.Abele, “Towards high build rates, combining different layer thicknesses within one part in selective laser melting”, *Proceedings of the 29th Annual International Solid Freeform Fabrication Symposium – An Additive Manufacturing Conference*, 2018.

[2] D.Buchbindera, H.Schleifenbaumb, S.Heidrichb, W.Meinersb, J.Bültmann, “High Power Selective Laser Melting (HP SLM) of Aluminum Parts”, *Physics Procedia*, vol. 12, Part A, pp. 271-278, 2011.

[3] H.Bikas, P.Stavropoulos, G.Chryssolouris, “Additive manufacturing methods and modeling approaches: A critical review”, *The International Journal of Advanced Manufacturing Technology*, vol.83, 1, July 2015.

[4] J.Metelkova, Y.Karolien, K.kempen, C.Formanoir, A.Witvrouw, B.V.Hooreweder, “On the influence of laser defocusing in Selective Laser Melting of 316L”, *Additive Manufacturing*, vol 23, pp 161-169, October 2018.

[5] Reports and Data, “Additive Manufacturing Market Analysis By Material Type (Metals, Thermoplastics, Ceramics, Others), By Metal Type (Titanium, Stainless Steel, High-Performance Alloys, Aluminum, Precious Metals, Others), By Polymer Type, By Ceramics Type, By Process, By End-use, And Segment Forecasts To 2027”, August 2020.

[6] E.Tempelman, H.Shercliff, B.N.Eyben, “Additive Manufacturing”, *Manufacturing and Design*, 11, pp 187-200, 2014.

[7] B. Schoinochoritis, D. Chantzis, K. Salonitis, “Simulation of metallic powder bed additive manufacturing processes with the finite element method, a critical review”, *Proceedings of the Institution of Mechanical Engineering, Part B: Journal of Engineering Manufacture*, Vol. 231, 1, 2017.

[8] M.Marke, C.Körner, "Multiscale Modeling of Powder Bed–Based Additive Manufacturing", *Annual Review of Materials Research*, July 2016.

[9] Z.J.Sun, X.P.Tan, S.Beng, T.Wai, Y.Yeong, “Selective laser melting of stainless steel 316L with low porosity and high build rates”, *Materials and Design*, vol.104, pp.197-204, August 2016.

[10] C.Chu, G.Graf, D.W.Rosen, “Design for additive manufacturing of cellular structures”, *Computational-Aided Design Application*, vol.5, 5, pp. 686-696, 2018.

[11] A.A.Zadpoor, "Mechanical performance of additively manufactured meta- biomaterials", *ActaBiomater*, 2018.

[12] E.Alabort, D.Barba, R.C.Reed, "Design of metallic bone by additive manufacturing", *Scripta Materialia*, vol.164, pp.110-114, 2019.

[13] J.G.Ge, J.Huang, Y.P.Lei, P.O.Reilly, M.Ahmed, C.Zhang, X.C.Yan, S.Yin, “Microstructural features and compressive properties of SLM Ti6Al4V lattice structures”, *Surface and Coatings Technology*, vol.403, December 2020.

[14] M.Dallago,"Effect of the geometrical defectiveness on the mechanical properties of SLM biomedical Ti6Al4V lattices", *Procedia Structural Integrity*, vol.13, 2018.

[15] M.Leary, "Inconel 625 lattice structures manufactured by selective laser melting (SLM), Mechanical properties, deformation and failure modes", *Materials and Design*, vol.157, 2018.

[16] T.Purtonen, A.Kalliosaari, A.Salminen, "Monitoring and adaptive control of laser processes", *Physics Procedia*, vol.56, pp.1218-1231, 2014.

[17] Y.Yang, M.F.Knol, F.van Keulen, C.Ayas, "A semi-analytical thermal modelling approach for selective laser melting", *Additive Manufacturing*, vol.21, pp.284-297, 2018.

[18] Y.Yang, F.van Keulen, C.Ayas, "A computationally efficient thermal model for selective laser melting", *Additive Manufacturing*, vol.31, 2020.

[19] P.R.Guduru, E.Chason, L.B.Freund, "Mechanics of compressive stress evolution during thin film growth", *Journal of the Mechanics and Physics of Solids*, vol.51, 2003.

[20] D.Thomas, "The Development of Design Rules for Selective Laser Melting", *Ph.D. Thesis, University of Wales*, 2009.

[21] T.Maconachie, M.Leary, B.Lozanovski, X.Z.Zhang, M.Qian, O.Faruque, M.Brandt, "SLM lattice structures: Properties, performance, applications and challenges", *Materials and Design*, vol.183, December 2019.

[22] B.Lozanovski, M.Leary, P.Tran, D.Shidid, M.Qian, P.Choong, M.Brandt, "Computational modelling of strut defects in SLM manufactured lattice structures", *Materials and Design*, vol.171, June 2019.

[23] M.Zheng, L.Wei, J.Chen, Q.Zhang, J.Q.Li, S.Sui, G.Wang, W.D.Huang, "Surface morphology evolution during pulsed selective laser melting: Numerical and experimental investigations", *Applied Surface Science*, vol.496, December 2019.

[24] Z.K.Wang, M.B.Liu, "Dimensionless analysis on selective laser melting to predict porosity and track morphology", *Journal of Materials Processing Technology*, vol.273 2019.

[25] Malvern Panalytical, "Powder bed fusion".

[26] Y.F.Tian, L.J.Yang, D.J.Zhao, Y.M.Huang, J.J.Pan, "Numerical analysis of powder bed generation and single track forming for selective laser melting of SS316L stainless steel", *Journal of Manufacturing Processes*, vol.58, pp.964-974, October 2020.

[27] Y.C.Wu, C.H.San, C.H.Chang, H.J.Lin, R.Marwand, S.Babad, W.S.Hwanga, "Numerical modeling of melt-pool behavior in selective laser melting with random powder distribution and experimental validation", *Journal of Materials Processing Technology*, vol.254, pp.72-78, April 2018.

[28] Y.S.Lee, W.Zhang, "Mesoscopic simulation of heat transfer and fluid flow in laser powder bed additive manufacturing; Proceedings of the Annual International Solid Freeform Fabrication Symposium", August 2015.

[29] W.J.Ge, S.W.Han, S.J.Nab, J.Y.H.Fuha, "Numerical modelling of surface morphology in selective laser melting", *Computational Materials Science*, vol.186, January 2021.

[30] Z.B.Luo, Y.Y.Zhao, "A survey of finite element analysis of temperature and thermal stress fields in powder bed fusion Additive Manufacturing", *Additive Manufacturing*, vol.21, pp.318-332, May 2018.

[31] P.R.Fische, V.Romano, H.Weber, N,Karapatis, E.Boillat, R.Glardon, "Sintering of commercially, pure titanium powder with a Nd,YAG laser source", *Acta Materialia*, vol.51, pp.1651–1662, 2003.

[32] L.Cao, "Numerical simulation of the impact of laying powder on selective laser melting single-pass formation", *International Journal of Heat and Mass Transfer*, vol.141, pp.1036-1048, October 2019.

[33] P.Yuan, D.Gu, "Molten pool behaviour and its physical mechanism during selective laser melting of TiC/AlSi10Mg nanocomposites, simulation and experiments", *Journal of Physics D: Applied Physics*, vol.48, pp.35303, 2015.

[34] C.Tang, J.L.Tan, C.H.Wong, "A numerical investigation on the physical mechanisms of single track defects in selective laser melting", *International Journal of Heat and Mass Transfer Part B*, vol.126, pp.957-968, November 2018.

[35] T.Voisin, N.P.Calta, S.A.Khairallah, J.Forien, L.Balogh , R.W.Cunningham, "Defects-dictated tensile properties of selective laser melted Ti-6Al-4V", *Materials and Design* , vol.158, pp.113-126, 2018.

[36] T.Mede, A.Kocjan, I.Paulin, M.Godec, "Numerical Mesoscale Modelling of Microstructure Evolution during Selective Laser Melting", *Metals*, vol.10, 6, June 2020.

[37] L.Cao, "Workpiece-scale numerical simulations of SLM molten pool dynamic behavior of 316L stainless steel", *Computers and Mathematics with Applications*, May 2020.

[38] W.T.Yan, S.Lin, O.L.Kafka, C.Yu, Z.L.Liu, Y.P.Lian, S.Wolff, J.Cao, G.J.Wagner, W.K.Liu, "Modeling process-structure-property relationships for additive manufacturing", *Frontiers of Mechanical Engineering*, vol.13, 4, pp.482-492, 2018.

[39] R.Ganeriwala, T.I.Zohdi, "A coupled discrete element-finite difference model of selective laser sintering", *Granular Matter*, 2018.

[40] C.Panwisawas, C.L.Qiu, M.J.Anderson, Y.Sovani, R.P.Turner, M.M.Attallah, J.W.Brooks, H.C.Basoalto, "Mesoscale modelling of selective laser melting: Thermal fluid dynamics and microstructural evolution", *Computational Materials Science*, vol.126, pp.479-490, January 2017.

[41] S.J.Wolff, S.Lin, E.J.Faierson, W.KLiu, Gregory. J.Wagner, J.Cao, "A framework to link localized cooling and properties of directed energy deposition (DED)-processed Ti-6Al-4V", *Acta Materialia*, vol.132, pp.106-117, June 2017.

[42] D.H.Dai, D.D.Gu, "Tailoring surface quality through mass and momentum transfer modeling using a volume of fluid method in selective laser melting of TiC/AlSi10Mg powder", *International Journal of Machine Tools and Manufacture*, vol.88, pp.95-107, January 2015.

[43] B.L.Van, G.Vansteenkiste,J.C.Boyer, "Comparisons of numerical modelling of the Selective Laser Melting", *Key Engineering Materials*, pp.504–506; 1067–1072, 2012.

[44] N.Contuzzi, S.L.Campanelli, A.D.Ludovico, "3D finiteelement analysis in the Selective Laser Melting process", *International Journal of Simulation Modelling*, vol.10, 3, pp.113–121, 2011.

[45] L.Ma, H.Bin, "Temperature and stress analysis andsimulation in fractal scanning-based laser sintering", *The International Journal of Advanced Manufacturing Technology*, vol.34, pp.898–903, 2007.

[46] S.Kolossov, E.Boillat, R.Glardon, "3D FE simula-tion for temperature evolution in the selective laser sinter-ing process", *International Journal of Machine Tools and Manufacture*, vol.44, pp.117–123, 2004.

[47] B.Song, S.Dong, H.Liao, "Process parameter selec-tion for selective laser melting of Ti6Al4V based on tem-perature distribution simulation and experimentalsintering",*The International Journal of Advanced Manufacturing Technology*, vol.61, PP.967–974, 2012.

[48] I.A.Roberts, C.J.Wang, R.Esterlein, "A three-dimensional finite element analysis of the temperaturefield during laser melting of metal powders in additivelayer manufacturing", *International Journal of Machine Tools and Manufacture*, vol.49, pp.916–923, 2009.

[49] S.Kolossov, E.Boillat, R.Glardon, "3D FE simula-tion for temperature evolution in the selective laser sinter-ing process", *International Journal of Machine Tools and Manufacture*, vol.44, pp.117–123,2004.

[50] C.Korner, E.Attar, P.Heinl, "Mesoscopic simulationof selective beam melting processes", *Journal of Materials Processing Technology*, vol.211, 6, pp.978–987, 2011.

[51] P.Michaleris, "Modeling metal deposition in heat transfer analyses of additive manufacturing processes", *Finite Elements in Analysis and Design*, vol.86, 2014.

[52] I.A.Roberts, "Investigation of Residual Stresses in the Laser Melting of Metal Powders in Additive Layer Manufacturing", *University of Wolverhampton West Midlands*, 2012.

[53] C.H.Fu, Y.B.Guo, "Three-Dimensional Temperature Gradient Mechanism in Selective Laser Melting of Ti-6Al-4V", *Journal of Manufacturing Science and Engineering*, December 2014.

[54] R.Li, Y.Shi, J.Liu, "Effects of processing parameters on the temperature field of selective laser melting metal powder", *Powder Metallurgy and Metal Ceramics*, vol.48, pp.186-195, 2009.

[55] I.Yadroitsev, P.Krakhmalev, I.Yadroitsava, "Selective Laser Melting of Ti6Al4V Alloy for Biomedical Applications: Temperature Monitoring and Microstructural Evolution",*Journal of Alloys and Compounds*, vol.583, pp.404-409, 2014.

[56] A.Hussein, L.Hao, C.Yan, R.Everson, "Finite element simulation of the temperature and stress fields in single layers built without-support in selective laser melting", *Materials and Design*, vol.52, pp.638–47, 2013.

[57] K.Antony, N.Arivazhagan, K.Senthilkumaran, "Numerical and experimental investigations on laser melt-ing of stainless steel 316L metal powders", *Journal of Manufacturing Processes*, vol.16, 3, pp.345–355, 2014.

[58] M.Chiumenti, E.Neiva, E.Salsi, M.Cervera, S.Badia, J.Moya, Z.E.Chen, C.Lee, C.Davies, "Numerical modelling and experimental validation in selective laser melting", *Additive Manufacturing*, vol.18, pp.171-185, December 2017.

[59] J.Crank, "Free and Moving Boundary Problems", *Oxford Science Publications*, 1984.

[60] T.Azad, L.Andallah, "Stability analysis of finite difference schemes for an advection diffusion equation", *The Bangladesh journal of scientific research*, 2017.

[61] D.Buchbinder, H.Schleifenbaum, S.Heidrich, W.Meiners, J.Bültmann, "High Power Selective Laser Melting (HP SLM) of Aluminum Parts", *Physics Procedia:Part A*, vol.12, pp.271-278, 2011.

A

Appendix

A

CALCULATION OF THE AVERAGE STRUT ORIENTATION OF A LATTICE

For a lattice structure, its average orientation of struts is calculated according to the length and orientation of its struts by the following equation,

$$\text{Average orientation} = \frac{\sum_{i=1}^{n} L_i \theta_i}{\sum_{i=1}^{n} L_i}, \tag{A.1}$$

where n represents the total number of the struts, L gives the length of the strut, θ is the orientation of the strut. Specifically, considering a square lattice with a rotation angle of 0 degree, which refers to its initial state as given in Figure A.1, it is formed from 42 mm vertical struts and 48 mm horizontal struts. Herein, the average orientation of this lattice structure is determined as,

$$\frac{90 \times 42 + 0 \times 48}{42 + 48} = 42 \text{degrees}. \tag{A.2}$$

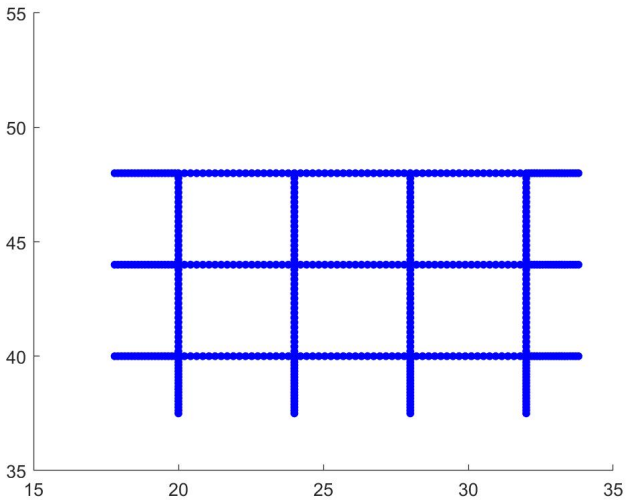

Figure A.1: Geometric graph of the 2D square lattice with rotation angle 0°. Herein its total number of connectivity (N_c) is 54.

Similarly, for the other cases listed in Table A.1 with varying lattice rotation angles, the calculation of their average strut orientations is listed as following,

Furthermore, the simulated temperature distribution of the lattice structures mentioned in this section, which are the lattice structure with different rotation angles from 0° to 75°, are shown in Figure (a) to (f), respectively.

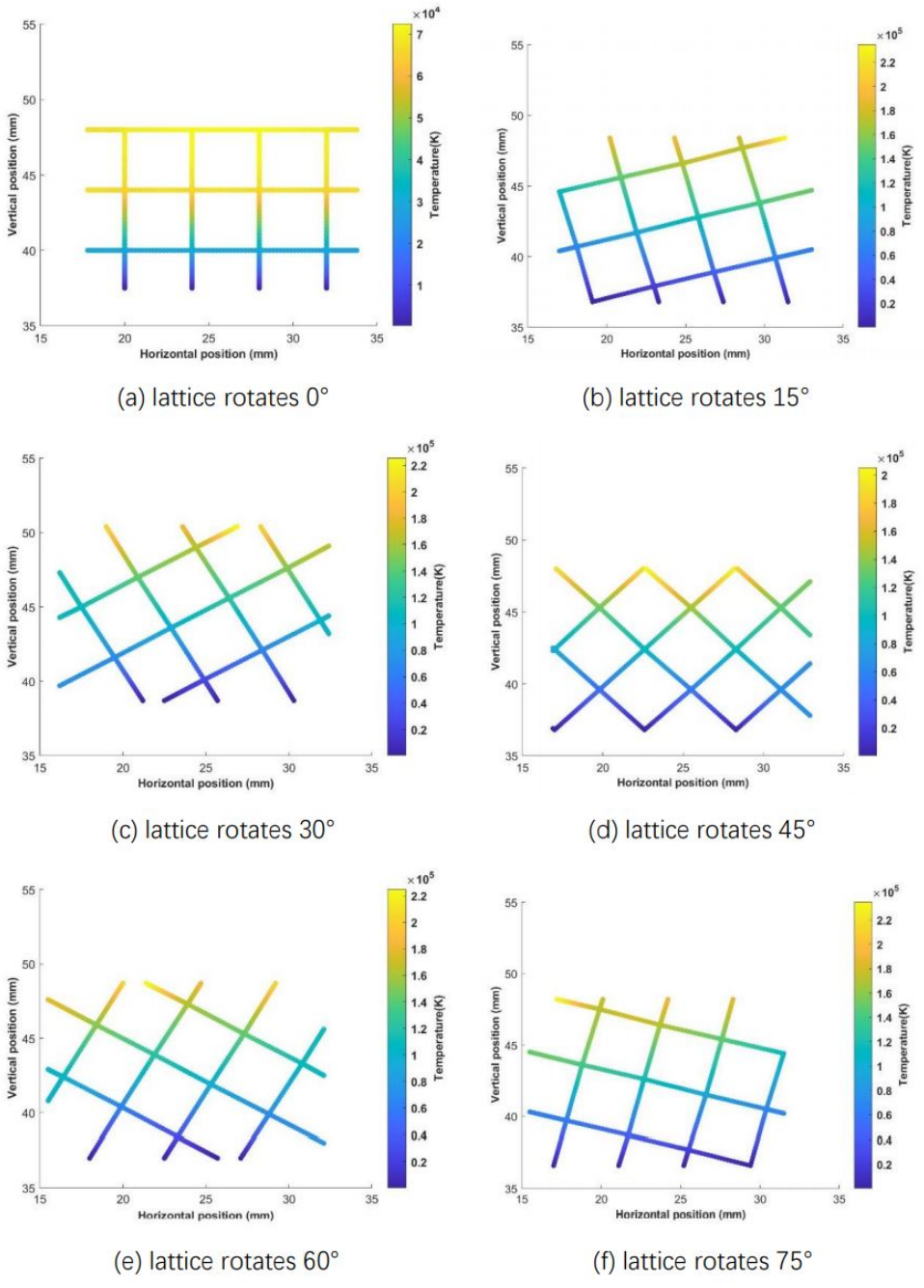

Figure A.2: Schematic description of temperature distribution of square lattice structures with varying rotation angle. (a) to (f) represent the lattice rotating 0°, 15°, 30°, 45°, 60°, and 75°, respectively.

A

Table A.1: The characteristic lengths of struts for a lattice structure are classified associated with the orientation of struts. Herein the square lattice with rotation angle from 15° to 75° are involved in this table, and their average strut orientation are determined.

Lattice rotation angle (degrees)	Characteristics of struts	Average orientation of members (degrees)
15	15°: 45.7507 mm 105°: 44.1025 mm	59.1746
30	30°: 42.4716 mm 120°: 45.1999 mm	76.4004
45	45°: 44.9047 mm 135°: 44.9031 mm	89.9992
60	60°: 46.0061 mm 150°: 43.3276 mm	103.6508
75	75°: 44.1025 mm 165°: 45.7507 mm	102.8254

B

Appendix

B

STABILITY CONDITION CALCULATION

The linear advection diffusion equation (ADE) describes the contaminant transport due to combined effect of advection and diffusion in a porous media, which is expressed as,

$$\frac{\partial c}{\partial t} + u\frac{\partial c}{\partial x} = D\frac{\partial^2 c}{\partial x^2}, \tag{B.1}$$

where $c(x, y, z, t)$ is the concentration (mass per unit volume) of pollutant at point (x, y, z) in Cartesian coordinates, at time t. The vector u is the fluid velocity field and D is the eddy diffusivity or dispersion tensor. The derivatives in the Eq.B.1 can be approximated by truncated Taylor Series expansions as follows,

$$\frac{\partial c}{\partial t} = \frac{c_i^{n+1} - c_i^n}{\Delta t} \text{ (1st order forward difference in time)}, \tag{B.2}$$

$$\frac{\partial c}{\partial x} = \frac{c_{i+1}^n - c_{i-1}^n}{2\Delta x} \text{ (1st order centered space difference formula)}, \tag{B.3}$$

$$\frac{\partial^2 c}{\partial x^2} = \frac{c_{i+1}^n - 2c_i^n + c_{i-1}^n}{\Delta x^2} \text{ (2nd order centered space difference formula)}. \tag{B.4}$$

Substituting the above equations Eq. B.2, Eq.B.3, and Eq.B.4 into Eq.B.1, we obtain,

$$\frac{c_i^{n+1} - c_i^n}{\Delta t} + u\frac{c_{i+1}^n - c_{i-1}^n}{2\Delta x} = D\frac{c_{i+1}^n - 2c_i^n + c_{i-1}^n}{\Delta x^2}, \tag{B.5}$$

and this implies that,

$$c_i^{n+1} = \left(\frac{\gamma}{2} + \lambda\right) c_{i-1}^n + (1 - 2\lambda)\, c_i^n + \left(\lambda - \frac{\gamma}{2}\right) c_{i+1}^n, \tag{B.6}$$

where,

$$\gamma = \frac{u\Delta t}{\Delta x}, \tag{B.7}$$

$$\lambda = \frac{D\Delta t}{\Delta x^2}. \tag{B.8}$$

For stability, Eq.B.6 must satisfy the conditions as follows,

$$0 \le \frac{\gamma}{2} + \lambda \le 1, \tag{B.9}$$

$$0 \le 1 - 2\lambda \le 1, \tag{B.10}$$

$$0 \le \lambda - \frac{\gamma}{2} \le 1. \tag{B.11}$$

Rearranging the equations from Eq.B.9 to Eq.B.10, we get,

$$0 \le \lambda \le \frac{1}{2}, \tag{B.12}$$

$$-2\lambda \le \gamma \le 2(1 - \lambda). \tag{B.13}$$

Based Eq.B.7 and Eq.B.8, the stability conditions Eq.B.12 and Eq.B.13 can be rewritten as,

$$0 \le \frac{D\Delta t}{\Delta x^2} \le \frac{1}{2}, \tag{B.14}$$

$$-2\frac{D\Delta t}{\Delta x^2} \le \frac{u\Delta t}{\Delta x} \le 2\left(1 - \frac{D\Delta t}{\Delta x^2}\right). \tag{B.15}$$

Consider now the governing equations for the thermal evolution of the lattice members analyzed in this work. There are several cases need to be involved as follows, Firstly, consider now an oblique strut. For a growing strut during the heating stage, its governing equation Eq.3.44 gives that,

$$D = \frac{1}{H^2}, \tag{B.16}$$

$$u = -\frac{\dot{H}}{H}\zeta, \tag{B.17}$$

so that,

$$0 \leq \frac{\Delta\tau}{H^2\Delta\zeta^2} \leq \frac{1}{2}, \tag{B.18}$$

$$-2\frac{\Delta\tau}{H^2\Delta\zeta^2} \leq -\frac{\dot{H}\Delta\tau}{H\Delta\zeta} \leq 2(1-\frac{\Delta\tau}{H^2\Delta\zeta^2}), \tag{B.19}$$

it follows that,

$$\Delta\tau \leq \frac{H^2\Delta\zeta^2}{2}, \tag{B.20}$$

$$\Delta\tau \leq \frac{2H^2\Delta\zeta^2}{2-\dot{H}H\zeta\Delta\zeta}, \tag{B.21}$$

for a growing strut during the cooling stage or a stationary strut, its governing equation Eq.3.45 gives that,

$$D = \frac{1}{H^2}, \tag{B.22}$$

$$u = 0, \tag{B.23}$$

then the corresponding stability conditions are,

$$0 \leq \frac{\Delta\tau}{H^2\Delta\zeta^2} \leq \frac{1}{2}, \tag{B.24}$$

$$0 \leq 2(1-\frac{\Delta\tau}{H^2\Delta\zeta^2}), \tag{B.25}$$

it follows that,

$$\Delta\tau \leq \frac{H^2\Delta\zeta^2}{2}, \tag{B.26}$$

$$\Delta\tau \leq 2H^2\Delta\zeta^2. \tag{B.27}$$

Next, consider now a horizontal strut. For a horizontal strut in different cases, the corresponding governing equations Eq.3.46 to Eq.3.48 are all imply that,

$$D = \beta^2, \tag{B.28}$$

$$u = 0, \tag{B.29}$$

similarly,

$$0 \leq \frac{\beta^2\Delta\tau}{\Delta X^2} \leq \frac{1}{2}, \tag{B.30}$$

$$0 \leq 2(1-\frac{\beta^2\Delta\tau}{\Delta X^2}), \tag{B.31}$$

thus,

$$\Delta\tau \leq \frac{\Delta X^2}{2\beta^2}, \tag{B.32}$$

$$\Delta\tau \leq \frac{\Delta X^2}{\beta^2}. \tag{B.33}$$